A thermo-hydro-mechanical model for energy piles under cyclic thermal loading

Arzanfudi, Mehdi M.; Al-Khoury, Rafid; Sluys, L.J.; Schreppers, G.M.A

DOI
10.1016/j.compgeo.2020.103560

Publication date
2020

Document Version
Final published version

Published in
Computers and Geotechnics

Citation (APA)
Arzanfudi, M. M., Al-Khoury, R., Sluys, L. J., & Schreppers, G. M. A. (2020). A thermo-hydro-mechanical model for energy piles under cyclic thermal loading. *Computers and Geotechnics*, *125*, Article 103560. https://doi.org/10.1016/j.compgeo.2020.103560

Computers and Geotechnics 125 (2020) 103560

Contents lists available at ScienceDirect

Computers and Geotechnics

journal homepage: www.elsevier.com/locate/compgeo

Research Paper

A thermo-hydro-mechanical model for energy piles under cyclic thermal loading

Mehdi M. Arzanfudi[a,*], Rafid Al-Khoury[a], L.J. Sluys[a], G.M.A. Schreppers[b]

[a] Faculty of Civil Engineering and Geosciences, Delft University of Technology, P.O. Box 5048, 2600 GA Delft, the Netherlands
[b] DIANA FEA BV, Thijsseweg 11, 2629JA Delft, Netherlands

ARTICLE INFO

Keywords:
Energy pile modeling
THM model
Embedded finite element
Pile-soil interface
Geothermal heat exchanger
Multiphase mixture material

ABSTRACT

This paper introduces a thermo-hydro-mechanical finite element model for energy piles subjected to cyclic thermal loading. We address four particular features pertaining to the physics of energy piles: three-dimensionality, embedded heat exchangers, soil constitutive modeling and pile–soil interface. The model is designed to capture the strong coupling between all important physical and thermomechanical processes occurring in a concrete pile embedding U-tubes heat exchangers and surrounded by a saturated soil mass. It encompasses solid and fluid compressibility, fluid and heat flow, thermoplastic deformation of soil, buoyancy, phase change, volume change, pore expansion, melting point depression, cryogenic suction and permeability reduction due to ice formation. The model is distinct from existing energy pile models in at least two features: (1) it can simulate the detailed convection-conduction heat flow in the heat exchanger and the associated unsymmetrical thermal interactions with concrete and soil mass; and (2) it can simulate cyclic freezing and thawing in the system and the associated changes in physical and mechanical properties of the soil mass that likely lead to thermoplasticity and deterioration of pile shaft resistance. The performance of the model is demonstrated through a numerical experiment addressing all its features.

1. Introduction

An energy pile (also known as thermal pile) is a dual-purpose structural element, functioning as a structural foundation and a ground source heat exchanger. This technology is appealing because it makes use of shallow depths to extract renewable energy suitable for heating and cooling of buildings. It reduces the use of fossil fuels and mitigates CO_2 emissions, and, compared to the conventional borehole heat exchanger, reduces installation costs and saves space. Nonetheless, construction companies are reluctant to apply this technology in daily practice because engineers are yet striving for more insight into the consequences of adding heat exchangers inside the pile on its structural functionality and the integrity of the pile–soil interface. Furthermore, so far, there is no compelling understanding of the long term behavior of energy piles when subjected to extreme operational scenarios leading to cyclic freezing and thawing. Current design methods do not account for the detailed thermal interaction between the heat exchangers and concrete, neither for the cyclic thermal loading and its effect on the thermo–hydro–mechanical behavior of soil and pile–soil interface.

Despite the increasing use of this technology, there are relatively few numerical models designed to study the thermo–hydro–mechanical (THM) behavior of energy piles and their surrounding soil mass. Several notable THM studies have been introduced, including those by Yavari et al. [35], Di Donna and Laloui [12], Gawecka et al. [16] and Anongphouth et al. [3]. They model energy piles with different levels of physical complexity, material constitutive relationships and pile–soil interaction.

A common feature of these studies is that they simulate the heat exchanger as a line heat source with a constant heat flux or a prescribed temperature. Normally, the heat exchanger is a U-tube, ~25 mm in diameter, made of high-grade polyethylene, fixed on the reinforcement cage inside the concrete pile. The heating (cooling) system works by circulating a fluid through the U-tube that collects (rejects) heat arising from a series of thermal interactions between the fluid, pipe wall, concrete and surrounding soil mass. These distinct geometrical and physical features are ignored in the line heat source approach, eliciting three main shortcomings: (1) it ignores the conductive-convective heat flow in the U-tube that varies following the daily and seasonal thermal load demands; (2) it ignores the three-dimensionality of the problem which results from the U-tubes configuration and their associated unsymmetrical heat flow and thermal stresses; and (3) it does not allow assessing the energy efficiency of the energy pile, which constitutes the

* Corresponding author.
E-mail address: M.MusivandArzanfudi@tudelft.nl (M.M. Arzanfudi).

https://doi.org/10.1016/j.compgeo.2020.103560
Received 31 January 2020; Received in revised form 12 March 2020; Accepted 19 March 2020
Available online 02 July 2020

main goal of using this technology.

The effect of temperature on the soil material parameters and its structural behavior constitutes the main disparity of energy piles from the conventional concrete piles, and hence given a special treatment in these studies. Yavari et al. [35], Gawecka et al. [16], and Anongphouth et al. [3] adopt constitutive relationships similar to those used in conventional soil mechanics; i.e. without specifically taking the temperature effects on the soil material parameters into account. However, the thermo-hydro-mechanical behavior of the soil mass is considered via the balance equations. Laloui and his co-workers [18,24,14,25], on the other hand, do consider the temperature effect on the soil material parameters. They introduced a phenomenological constitutive modeling approach based on continuum thermoplasticity. We briefly discuss this approach in Section 2.

The pile–soil interaction is another important aspect in energy pile design, currently treated with different levels of complexity. Gawecka et al. [16] and Yavari et al. [35] do not model the interface between the pile and soil. The pile finite elements share the same nodes with the soil elements, inhibiting thus any relative displacement between them. Anongphouth et al. [3], on the other hand, model the interface between the pile and soil, but adopt a constitutive model for the interface element similar to the surrounding soil mass, i.e. the soil in the interface has the same strength as the soil mass, but can exhibit relative displacement. Suryatriyastuti et al. [32] employ frictional interface elements based on the Mohr-Coulomb failure criterion. Sutman et al. [33] use thin-layer elements with elastic properties to model the pile–soil interface. Di Donna and Laloui [12] use a thin-layer element based on their ACMEG-T model (Advanced Constitutive Model for Environmental Geomechanics), but the same constitutive parameters as those used for the surrounding soil. Rotta Loria et al. [29], Rotta Loria et al. [30], and Di Donna et al. [13] have employed more advanced thin-layer elements based on the thermo-elastoplastic Mohr-Coulomb failure criterion with reduced mechanical properties compared to the surrounding soil.

In this paper, we address these three aspects of energy piles: heat exchangers, soil constitutive behavior and pile–soil interaction, together with the three-dimensionality of the problem. We introduce a 3D finite element model describing the THM behavior of an energy pile system subjected to cyclic thermal loads. Details of the modeling approach are given hereafter.

2. Modeling approach

In a previous work, the authors introduced a detailed thermo-hydro-mechanical computational model for freezing and thawing in porous media [5]. It is formulated based on the averaging theory and discretized using axial-symmetric finite elements. The model is capable of capturing the strong coupling between all important phenomena and processes occurring in the porous domain, including solid and fluid compressibility, fluid and heat flow, buoyancy, phase change, volume change, pore expansion, melting point depression, cryogenic suction and permeability reduction due to ice formation. Here, this model is customized to be used for energy piles, and tailored to consider four particular features: three-dimensionality, embedded heat exchangers, soil constitutive modeling, and pile–soil interface.

The energy pile is by definition three-dimensional (3D), pertaining to the configuration of the U-tube heat exchanger inside it (Fig. 1a). The temperature in pipe-in at cross sections along the pile is different than that in pipe-out (Fig. 1b). As the pile diameter is relatively large compared to the U-tube, the temperature gradient between pipe-in and pipe-out gives rise to radially unsymmetrical thermal stresses and strains in the pile and the surrounding soil mass. Furthermore, piles are usually installed in groups with arbitrary configurations, and thus, detailed modeling of pile groups must be three-dimensional. In this work, 3D brick and wedge finite elements are utilized for this purpose.

Heat flow in the heat exchanger is conductive–convective arising

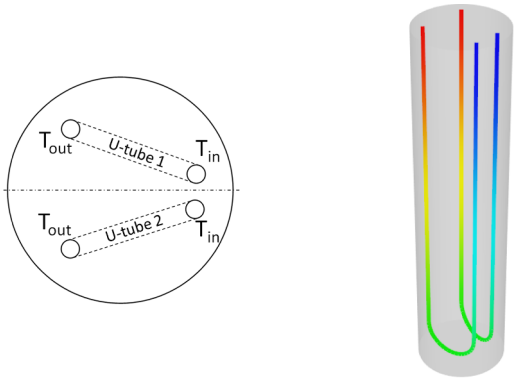

Fig. 1. Energy pile geometry and temperature: (a) typical energy pile cross section; (b) typical temperature profile in U-tubes.

from the thermal interaction between the circulating fluid in the U-tubes and the surrounding concrete and soil mass. The U-tube heat exchanger is relatively small in diameter (25 mm) which entails that the heat flow inside it is nearly one-dimensional (1D). This allows modeling heat flow in the U-tube by a line element with its thermal interaction with the pile expressed explicitly in the governing heat equation [1]. Here, the embedded finite element method is utilized to discretize the heat exchanger. Elements of this kind, can go through the host 3D elements, avoiding the need for fine meshes and keeping the mesh structured.

The soil is by definition a multiphase material constituting, basically, a solid matrix phase and a water phase. Within the temperature range of this application, the solid matrix, except for thermal expansion and contraction and its Young's modulus, is not significantly affected by the temperature variation. Rather, it is the water phase that is being affected: the temperature alters its mass density, heat capacity, thermal conductivity and viscosity. Additionally, the water might change phase, leading to changing soil strength, permeability and volume. Based on this, we adopt a multiphase mixture approach to formulate the constitutive relationships for the soil material. This approach is different than the phenomenological approach of Laloui and his co-workers [18,24,14,25], who consider the soil as a homogeneous porous matrix. The behavior of the soil in their approach is described by a thermo-elastoplastic model with a yield function expressed in the stress-temperature space, as shown schematically in Fig. 2a. This kind of models is basically appropriate for the soils under investigation, and any other type of soils must be examined experimentally to establish its parameters dependency on temperature. In our multiphase mixture approach, however, the soil is described by its constituents: a solid matrix and a water phase (Fig. 2b). Following this, the conventional constitutive relationships for soil can be utilized to model the solid matrix, and the equations of state (EOS) can be utilized to describe the water phase. We model the solid matrix using the modified Cam-Clay yield function, and the water using equations of state describing its pressure-temperature-volume relationships and the dependency of its physical parameters on temperature. The thermal dependency of soil is thus included fundamentally via the water EOS, together with the thermal expansion coefficient and temperature dependent Young's modulus of the solid matrix.

Understanding the behavior of the pile–soil interface is essential to prevent the deterioration of the pile shaft resistance and bearing capacity under the effect of cyclic thermal loads. We adopt the Desai thin-layer approach [11], but extending it to a multiphase mixture exhibiting sliding, debonding and volume change pertained to the induced thermo-hydro-mechanical forces. The interface material behavior is expressed using the Drucker-Prager yield function and the water EOS.

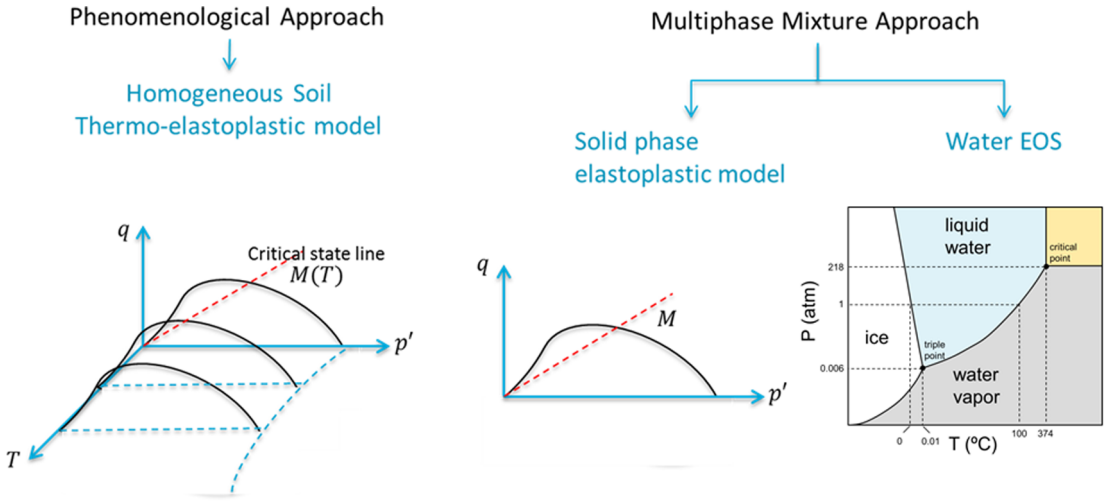

Fig. 2. Phenomenological versus multiphase mixture constitutive modeling approaches.

3. Governing equations

The physical domain consists of a concrete energy pile embedded in a soil mass and subjected to mechanical and cyclic thermal loads. The pile embeds U-tube heat exchangers exhibiting conduction-convection heat transfer due to the thermal interaction between the circulating fluid in the U-tube and the surrounding concrete. The concrete pile exhibits thermo-mechanical behavior due to the applied mechanical loads, the thermal interaction with the heat exchangers and the thermo-mechanical interaction with the surrounding soil mass. The soil mass exhibits thermo-hydro-mechanical behavior arising from the thermo-mechanical interaction with the concrete pile and the fluid flow due to consolidation, buoyancy and cryogenic suction in the soil body. The field equations governing these processes in the soil mass, concrete, pile–soil interface and heat exchanger are given hereafter.

3.1. Soil mass

The soil mass is considered saturated, isotropic and non-isothermal with local thermal equilibrium. It constitutes a multiphase mixture composing a solid matrix and water, which can change phase between liquid water and ice. The soil exhibits solid and fluid compressibility, heat and fluid flow, thermo-elastoplasticity, buoyancy, volume change, pore expansion, permeability change, cryogenic suction and melting point depression. The three phases (solid matrix, liquid water and ice) interact physically with each other and exchange mass, momentum and energy. The governing balance equations describing the conserved quantities in a multiphase porous medium domain are given in detail in Arzanfudi and Al-Khoury [5]. Here, we state the balance equations together with the constitutive relationships relevant to the energy pile system. They are expressed in terms of the primary state variables: solid matrix displacement $\boldsymbol{u}$, water mixture pressure p_m, water mixture specific enthalpy h_m, solid matrix temperature T_s, and cryogenic suction s_c.

3.1.1. Conservation of momentum

The averaged macroscopic linear momentum balance equation of a multiphase mixture constituting a solid matrix, a liquid water phase and an ice phase, and subjected to thermo-hydro-mechanical forces can be expressed in an incremental form as

$$\nabla\cdot[\mathrm{d}\boldsymbol{\sigma}' - \boldsymbol{m}\alpha\mathrm{d}p_s] + \mathrm{d}\rho_{eff}\boldsymbol{g} = 0 \tag{1}$$

where $\boldsymbol{\sigma}' = \boldsymbol{\sigma} + \boldsymbol{m}\alpha p_s$ is the effective stress, with $\boldsymbol{\sigma}$ being the total stress; α is Biot's coefficient; $\boldsymbol{m} = [1, 1, 1, 0, 0, 0]^T$; $\boldsymbol{g}$ is the gravitational vector; p_s is the pressure exerted by the water phase on the solid matrix, defined as

$$p_s = S_{lw}p_{lw} + S_{ice}p_{ice} \tag{2}$$

where p_{lw} and p_{ice} are the liquid water and ice pressures, and S_{lw} and S_{ice} are their degrees of saturation; and ρ_{eff} is the effective mass density, defined as

$$\rho_{eff} = (1-\varphi)\rho_s + \varphi S_{ice}\rho_{ice} + \varphi S_{lw}\rho_{lw} \tag{3}$$

in which φ is the porosity, ρ_s, ρ_{lw} and ρ_{ice} are the mass density of solid matrix, liquid water and ice, respectively.

The dependent variables in Eq. (1) are functions of the primary state variables, such that $p_s = p_s(p_m, h_m, s_c)$, and $\rho_{eff} = \rho_{eff}(p_m, h_m)$, with the subscript m denoting the water mixture (liquid water and ice). Using the chain rule, the derivatives of these dependent variables can be expressed as

$$\begin{aligned}\mathrm{d}p_s &= \frac{\partial p_s}{\partial h_m}\mathrm{d}h_m + \frac{\partial p_s}{\partial p_m}\mathrm{d}p_m + \frac{\partial p_s}{\partial s_c}\mathrm{d}s_c\\ \mathrm{d}\rho_{eff} &= \frac{\partial \rho_{eff}}{\partial h_m}\mathrm{d}h_m + \frac{\partial \rho_{eff}}{\partial p_m}\mathrm{d}p_m\end{aligned} \tag{4}$$

Substituting Eq. (4) into Eq. (1) gives

$$\nabla\cdot\left[\mathrm{d}\boldsymbol{\sigma}' - \boldsymbol{m}\alpha\left(\frac{\partial p_s}{\partial h_m}\mathrm{d}h_m + \frac{\partial p_s}{\partial p_m}\mathrm{d}p_m + \frac{\partial p_s}{\partial s_c}\mathrm{d}s_c\right)\right] + \left(\frac{\partial \rho_{eff}}{\partial h_m}\mathrm{d}h_m + \frac{\partial \rho_{eff}}{\partial p_m}\mathrm{d}p_m\right)\boldsymbol{g} = 0 \tag{5}$$

Eq. (5) is the equilibrium equation of the volume-averaged, compressible multiphase mixture of solid matrix, liquid water and ice.

Constitutive relationships

The effective stress increment in Eq. (5) is described as

$$\mathrm{d}\boldsymbol{\sigma}' = \boldsymbol{D}^{ep}\left(\boldsymbol{L}\mathrm{d}\boldsymbol{u} - \frac{1}{3}\boldsymbol{m}\beta_s\mathrm{d}T_s\right) \tag{6}$$

in which β_s is the volumetric thermal expansion coefficient of the solid matrix, $\boldsymbol{L}$ is the differential operator, and $\boldsymbol{D}^{ep}$ is the tangential elasto-plastic stiffness matrix of the solid matrix, described, as

$$\boldsymbol{D}^{ep} = \boldsymbol{D}^{e} - \frac{\boldsymbol{D}^{e}\dfrac{\partial Q}{\partial \boldsymbol{\sigma}'}\dfrac{\partial F}{\partial \boldsymbol{\sigma}'}^{T}\boldsymbol{D}^{e}}{-\dfrac{\partial F}{\partial \boldsymbol{\varepsilon}^{p}}^{T}\dfrac{\partial Q}{\partial \boldsymbol{\sigma}'} + \dfrac{\partial F}{\partial \boldsymbol{\sigma}'}^{T}\boldsymbol{D}^{e}\dfrac{\partial Q}{\partial \boldsymbol{\sigma}'}} \tag{7}$$

where F is a yield function, Q is a potential plastic function, $\boldsymbol{\varepsilon}^p$ is the plastic strain tensor, and $\boldsymbol{D}^e$ is the tangential elastic stiffness matrix, expressed, for a three-dimensional solid matrix, as

$$\boldsymbol{D}^e = \frac{E(T)}{(1+\nu)(1-2\nu)} \begin{bmatrix} 1-\nu & \nu & \nu & 0 & 0 & 0 \\ & 1-\nu & \nu & 0 & 0 & 0 \\ & & 1-\nu & 0 & 0 & 0 \\ & & & \frac{1-2\nu}{2} & 0 & 0 \\ & \text{Symmetric} & & & \frac{1-2\nu}{2} & 0 \\ & & & & & \frac{1-2\nu}{2} \end{bmatrix} \tag{8}$$

in which υ is Poisson's ratio, and $E(T)$ is a temperature-dependent elastic modulus, defined here as

$$E(T) = E_0 e^{-b(T_s - T_0)} \tag{9}$$

where E_0 is the Young's modulus at a reference temperature, T_0, and b is a material parameter.

For the relatively small thermo-hydro-mechanical strain level generated by the cyclic thermal loading, it is reasonable to assume that the soil behavior is governed by an isotropic hardening/softening rule with an associated flow rule, giving $Q = F$ in Eq. (7). The modified Cam-Clay yield function is utilized for this purpose. In the $p-q$ stress space, it is expressed as

$$F = \frac{q^2}{M_{cs}^2} + p(p - p_c) = 0 \tag{10}$$

in which p is the mean normal stress, q is the deviatoric stress, M_{cs} is the slope of the critical limit state line, p_c is the instantaneous consolidation pressure, defined as [26]

$$p_c = p_{c0}\, e^{\frac{1}{n}(\varepsilon_v^p - \varepsilon_{v0}^p)} \tag{11}$$

where p_{c0} is the pre-consolidation pressure, n is a material constant related to the hardening and softening of the material, ε_{v0}^p is the initial volumetric plastic strain, and $\varepsilon_v^p = \mathbf{m}^T\varepsilon^p$ is the volumetric plastic strain. The yield surface is smooth with an initial size governed by the magnitude of the pre-consolidation pressure (p_{c0}). The yield surface expands in size due to strain hardening arising from compaction, and shrinks in size due to strain softening resulting from volume increase. More details can be found in Chen and Baladi [9] and Lewis and Schrefler [26].

The consistency condition of the yield surface, Eq. (10), is

$$\left(\frac{\partial F}{\partial \boldsymbol{\sigma}'}\right)^T d\boldsymbol{\sigma}' + \left(\frac{\partial F}{\partial \varepsilon^p}\right)^T d\varepsilon^p = 0 \tag{12}$$

where

$$\frac{\partial F}{\partial \boldsymbol{\sigma}'} = \frac{\partial F}{\partial p}\frac{\partial p}{\partial \boldsymbol{\sigma}'} + \frac{\partial F}{\partial q}\frac{\partial q}{\partial \boldsymbol{\sigma}'} = \frac{p_c - 2p}{3}\begin{bmatrix}1\\1\\1\\0\\0\\0\end{bmatrix} + \frac{1}{M_{cs}^2}\begin{bmatrix}2\sigma_x' - \sigma_y' - \sigma_z'\\2\sigma_y' - \sigma_z' - \sigma_x'\\2\sigma_z' - \sigma_x' - \sigma_y'\\6\tau_{xy}\\6\tau_{yz}\\6\tau_{zx}\end{bmatrix}$$

$$\frac{\partial F}{\partial \varepsilon^p} = \frac{\partial F}{\partial p_c}\frac{\partial p_c}{\partial \varepsilon_v^p}\frac{\partial \varepsilon_v^p}{\partial \varepsilon^p} = \frac{p\, p_c}{n}\begin{bmatrix}1\\1\\1\\0\\0\\0\end{bmatrix} \tag{13}$$

and

$$d\varepsilon^p = d\lambda \frac{\partial F}{\partial \boldsymbol{\sigma}'} \tag{14}$$

which is the plastic strain increment defining an associated flow rule, with

$$d\lambda = -\frac{(\partial F/\partial \boldsymbol{\sigma}')^T d\boldsymbol{\sigma}'}{(\partial F/\partial \varepsilon^p)^T(\partial F/\partial \boldsymbol{\sigma}')} \tag{15}$$

The other constitutive relationships in Eq. (5) ($\partial \rho_s/\partial s_c$,$\partial \rho_{eff}/\partial h_m$, $\partial \rho_{eff}/\partial p_m$) can be found in Appendix C.

Momentum field equation

Substituting the constitutive equations into the momentum balance equation, Eq. (5), gives the momentum field equation of the solid matrix.

3.1.2. Conservation of mass

The averaged macroscopic mass balance equation for the multi-phase soil mixture is formulated by summing the mass conservation equations of the individual phases. ***Solidmatrix***

The mass balance equation for a homogeneous solid matrix phase can be described as

$$\frac{(1-\varphi)}{\rho_s}\frac{\partial \rho_s}{\partial t} - \frac{\partial \varphi}{\partial t} + (1-\varphi)\boldsymbol{m}^T\boldsymbol{L}\frac{\partial \boldsymbol{u}}{\partial t} = 0 \tag{16}$$

Following Lewis and Schrefler [26], the solid matrix mass density can be described as

$$\frac{1}{\rho_s}\frac{\partial \rho_s}{\partial t} = \frac{1}{1-\varphi}\left[(\alpha-\varphi)\frac{1}{K_s}\frac{\partial p_s}{\partial t} - \beta_s(\alpha-\varphi)\frac{\partial T_s}{\partial t} - (1-\alpha)\boldsymbol{m}^T\boldsymbol{L}\frac{\partial \boldsymbol{u}}{\partial t}\right] \tag{17}$$

in which K_s is the bulk modulus of the solid grains.

Using Eq. (4) for $p_s = p_s(p_m, h_m, s_c)$, and substituting into Eqs. (16) and (17), gives

$$\frac{\partial \varphi}{\partial t} = \frac{\alpha-\varphi}{K_s}\left(\frac{\partial p_s}{\partial h_m}\frac{\partial h_m}{\partial t} + \frac{\partial p_s}{\partial p_m}\frac{\partial p_m}{\partial t} + \frac{\partial p_s}{\partial s_c}\frac{\partial s_c}{\partial t}\right) - \beta_s(\alpha-\varphi)\frac{\partial T_s}{\partial t} - (\varphi-\alpha)\boldsymbol{m}^T\boldsymbol{L}\frac{\partial \boldsymbol{u}}{\partial t} \tag{18}$$

This equation reveals that the porosity is not constant and can be altered by the thermo-hydro-mechanical forces in the soil.

Liquid water phase

The mass balance equation for the liquid water phase can be expressed as

$$\frac{\partial \varphi}{\partial t} + \frac{\varphi}{\rho_{lw}}\frac{\partial \rho_{lw}}{\partial t} + \frac{\varphi}{S_{lw}}\frac{\partial S_{lw}}{\partial t} + \frac{1}{S_{lw}\rho_{lw}}\nabla\cdot(\rho_{lw}\boldsymbol{v}_{lw}) + \varphi\boldsymbol{m}^T\boldsymbol{L}\frac{\partial \boldsymbol{u}}{\partial t} = -\frac{\dot{m}_{lw\to ice}}{S_{lw}\rho_{lw}} \tag{19}$$

in which $\boldsymbol{v}_{lw}$ is the extrinsic averaged velocity of liquid water, and $\dot{m}_{lw\to ice}$ is the mass exchange rate arising from the phase change between the liquid water and ice.

Inserting Eq. (18) into Eq. (19) and expressing the liquid water density and saturation in terms of the state variables: $\rho_{lw}(p_m, h_m)$, $S_{lw}(p_m, h_m)$, yields

$$\begin{aligned}&\left(\frac{\alpha-\varphi}{K_s}S_{lw}\rho_{lw}\frac{\partial p_s}{\partial p_m} + \varphi S_{lw}\frac{\partial \rho_{lw}}{\partial p_m} + \varphi\rho_{lw}\frac{\partial S_{lw}}{\partial p_m}\right)\frac{\partial p_m}{\partial t}\\ &+\left(\frac{\alpha-\varphi}{K_s}S_{lw}\rho_{lw}\frac{\partial p_s}{\partial h_m} + \varphi S_{lw}\frac{\partial \rho_{lw}}{\partial h_m} + \varphi\rho_{lw}\frac{\partial S_{lw}}{\partial h_m}\right)\frac{\partial h_m}{\partial t}\\ &+\frac{\alpha-\varphi}{K_s}S_{lw}\rho_{lw}\frac{\partial p_s}{\partial s_c}\frac{\partial s_c}{\partial t} - \beta_s(\alpha-\varphi)S_{lw}\rho_{lw}\frac{\partial T_s}{\partial t}\\ &+\alpha S_{lw}\rho_{lw}\boldsymbol{m}^T\boldsymbol{L}\frac{\partial \boldsymbol{u}}{\partial t} + \nabla\cdot(\rho_{lw}\boldsymbol{v}_{lw}) = -\dot{m}_{lw\to ice}\end{aligned} \tag{20}$$

Ice phase

Similar to the liquid water phase in Eq. (20), the mass balance equation of the ice phase can readily be derived to give

$$\left(\frac{\alpha-\varphi}{K_s}S_{ice}\rho_{ice}\frac{\partial p_s}{\partial p_m}+\varphi S_{ice}\frac{\partial \rho_{ice}}{\partial p_m}+\varphi\rho_{ice}\frac{\partial S_{ice}}{\partial p_m}\right)\frac{\partial p_m}{\partial t}+$$
$$+\left(\frac{\alpha-\varphi}{K_s}S_{ice}\rho_{ice}\frac{\partial p_s}{\partial h_m}+\varphi S_{ice}\frac{\partial \rho_{ice}}{\partial h_m}+\varphi\rho_{ice}\frac{\partial S_{ice}}{\partial h_m}\right)\frac{\partial h_m}{\partial t}$$
$$+\frac{\alpha-\varphi}{K_s}S_{ice}\rho_{ice}\frac{\partial p_s}{\partial s_c}\frac{\partial s_c}{\partial t}-\beta_s(\alpha-\varphi)S_{ice}\rho_{ice}\frac{\partial T_s}{\partial t}$$
$$+\alpha S_{ice}\rho_{ice}\boldsymbol{m}^T\boldsymbol{L}\frac{\partial \boldsymbol{u}}{\partial t}+\nabla\cdot(\rho_{ice}\boldsymbol{v}_{ice})=\dot{m}_{lw\to ice} \tag{21}$$

in which $\boldsymbol{v}_{ice}$ is the extrinsic averaged velocity of ice, considered to be zero in this application ($\boldsymbol{v}_{ice}=0$).

Water mixture (liquid water and ice)

Considering the following identities:

$$S_{lw}+S_{ice}=1$$
$$\rho_m=S_{lw}\rho_{lw}+S_{ice}\rho_{ice} \tag{22}$$

and by summing Eqs. (20) and (21), assuming that the liquid water flow rate is governed by Darcy's law, and defining the water mixture pressure as $p_m=p_{lw}+s_c$, gives [5]:

$$\left(\frac{\alpha-\varphi}{K_s}\rho_m\frac{\partial p_s}{\partial p_m}+\varphi\frac{\partial \rho_m}{\partial p_m}\right)\frac{\partial p_m}{\partial t}+\left(\frac{\alpha-\varphi}{K_s}\rho_m\frac{\partial p_s}{\partial h_m}+\varphi\frac{\partial \rho_m}{\partial h_m}\right)\frac{\partial h_m}{\partial t}$$
$$-\rho_m\beta_s(\alpha-\varphi)\frac{\partial T_s}{\partial t}+\alpha\rho_m\boldsymbol{m}^T\boldsymbol{L}\frac{\partial \boldsymbol{u}}{\partial t}+\frac{\alpha-\varphi}{K_s}\rho_m\frac{\partial p_s}{\partial s_c}\frac{\partial s_c}{\partial t}$$
$$+\nabla\cdot\left(-\rho_{lw}\frac{\boldsymbol{k}k_{rlw}}{\mu_{lw}}\nabla p_m+\rho_{lw}\frac{\boldsymbol{k}k_{rlw}}{\mu_{lw}}\nabla s_c+\rho_{lw}\frac{\boldsymbol{k}k_{rlw}}{\mu_{lw}}\rho_{lw}\boldsymbol{g}\right)=0 \tag{23}$$

where μ_{lw} is the dynamic viscosity of liquid water, $\boldsymbol{k}$ is the absolute permeability, and k_{rlw} is the relative permeability. Eq. (23) is the continuity equation of the volume-averaged, compressible multiphase mixture of solid matrix, liquid water and ice with phase change.

Constitutive relationships:

Water equation of state (EOS)

The thermodynamic state variables and properties of the liquid water, ice and the water mixture, ρ_m, T_m, ρ_{ice}, ρ_{lw}, S_{ice}, S_{lw}, μ_{lw} are obtained from the equation of state of water, adopted from IAPWS [21] and other relevant literature, given in Appendix A.

Melting point depression

Kurylyk and Watanabe [23] presented an interesting review describing different forms of the Clapeyron equations and empirical relationships for soil freezing curves (SFC). Here, we adopt an exponential function of the form:

$$S_{lw}=S^*+(1-S^*)e^{a(T_m-T_f)} \tag{24}$$

in which S^* is the residual unfrozen water content at a relatively cold condition, T_f is the bulk freezing temperature, and a is a material constant.

Cryogenic suction

The cryogenic suction, s_c, exhibits a substantial change for each degree Celsius below zero. As a consequence, the cryogenic suction is considered here a primary state variable, to have it directly computed from solving the finite element equations, rather than being calculated in the post processing (see Arzanfudi and Al-Khoury [5] for more details). The computed quantity has to satisfy the Clausius-Clapeyron relation [26]:

$$s_c=-\rho_{ice}L_f\ln\frac{T_m}{T_f} \tag{25}$$

where L_f is the latent heat of fusion of water. To satisfy this condition, the following constraint is imposed:

$$-\rho_{ice}L_f\ln\frac{T_m}{T_f}\bigg|_{\text{Clausius - Clapeyron}}-s_c|_{\text{computed}}=0 \tag{26}$$

Relative permeability

Even though the domain is fully saturated, the water exhibits a phase change during freezing and thawing, giving rise to a quasi-partially saturated condition within the water phase. As for the partially saturated conditions, the relative permeability of liquid water is described based on the Brooks and Corey relationship [8]:

$$k_{rlw}=S_{lw}^{(2+3\eta)/\eta} \tag{27}$$

where η is a material constant.

Mass field equation

Substituting the constitutive relationships from Eqs. (24)–(27) and Appendices A and C into the macroscopic mass balance equation, Eq. (23), gives the mass field equation.

3.1.3. Conservation of energy

The averaged macroscopic energy balance equation for a multiphase mixture in local equilibrium is formulated by summing the heat equations of the solid matrix and the water mixture.

Solid matrix

$$\frac{\partial}{\partial t}[\rho_s c_s(1-\varphi)T_{sm}-(1-\varphi)p_s']+\nabla\cdot(\rho_s c_s\boldsymbol{v}_s T_{sm})+\nabla\cdot(1-\varphi)\boldsymbol{\lambda}_s\cdot\nabla T_{sm}=0 \tag{28}$$

in which T_{sm} is the solid matrix temperature and $\boldsymbol{\lambda}_s$ is its thermal conductivity.

Water mixture

$$\frac{\partial}{\partial t}[\rho_m\varphi h_m-\varphi p_m]+\nabla\cdot(\rho_m\boldsymbol{v}_m h_m)+\nabla\cdot\varphi\boldsymbol{\lambda}_m\cdot\nabla T_m=0 \tag{29}$$

Summing Eq. (28) to Eq. (29) and considering a thermal local equilibrium, $T_m=T_{sm}=T_s$, yields

$$\frac{\partial}{\partial t}[\rho_s c_s(1-\varphi)T_s+\rho_m\varphi h_m-(1-\varphi)p_s'-\varphi p_m]$$
$$+\nabla\cdot(\rho_s c_s\boldsymbol{v}_s T_s+\rho_m\boldsymbol{v}_m h_m)+\nabla\cdot\boldsymbol{\lambda}_{eff}\cdot\nabla T_s=0 \tag{30}$$

where

$$\boldsymbol{\lambda}_{eff}=(1-\varphi)\boldsymbol{\lambda}_s+\varphi\boldsymbol{\lambda}_m \tag{31}$$

is the effective thermal conductivity of the porous domain, with $\boldsymbol{\lambda}_s$ denoting the thermal conductivity of the solid matrix, and $\boldsymbol{\lambda}_m=S_{lw}\boldsymbol{\lambda}_{lw}+S_{ice}\boldsymbol{\lambda}_{ice}$, with $\boldsymbol{\lambda}_{lw}$ and $\boldsymbol{\lambda}_{ice}$ denoting the thermal conductivity of liquid water and ice, respectively.

Considering $\nabla\cdot\boldsymbol{v}_s=\boldsymbol{m}^T\boldsymbol{L}\frac{\partial \boldsymbol{u}}{\partial t}$, utilizing Eqs. (17) and (18), expressing Eq. (30) in terms of the primary state variables, and expanding the derivatives, leads to

$$[(1-\varphi)\rho_s c_s-\beta_s(\alpha-\varphi)(\rho_m h_m-p_m+p_s')]\frac{\partial T_s}{\partial t}$$
$$+\left[\varphi\rho_m+\varphi h_m\frac{\partial \rho_m}{\partial h_m}+(\rho_m h_m-p_m+p_s')\frac{\alpha-\varphi}{K_s}\frac{\partial p_s}{\partial h_m}\right]\frac{\partial h_m}{\partial t}$$
$$+\left[(\rho_m h_m-p_m+p_s')\frac{\alpha-\varphi}{K_s}\frac{\partial p_s}{\partial p_m}-\varphi+\varphi h_m\frac{\partial \rho_m}{\partial p_m}\right]\frac{\partial p_m}{\partial t}$$
$$+[(1-\varphi)K_T-(\varphi-\alpha)\rho_m h_m-(\varphi-\alpha)(-p_m+p_s')]\boldsymbol{m}^T\boldsymbol{L}\frac{\partial \boldsymbol{u}}{\partial t}$$
$$+(\rho_m h_m-p_m+p_s')\frac{\alpha-\varphi}{K_s}\frac{\partial p_s}{\partial s_c}\frac{\partial s_c}{\partial t}$$
$$+\nabla\cdot\left[-\rho_{lw}h_{lw}\frac{\boldsymbol{k}k_{rlw}}{\mu_{lw}}\nabla p_m+\rho_{lw}h_{lw}\frac{\boldsymbol{k}k_{rlw}}{\mu_{lw}}\nabla s_c-\boldsymbol{\lambda}_{eff}\nabla T_s+\rho_{lw}h_{lw}\frac{\boldsymbol{k}k_{rlw}}{\mu_{lw}}\rho_{lw}\boldsymbol{g}\right]=0 \tag{32}$$

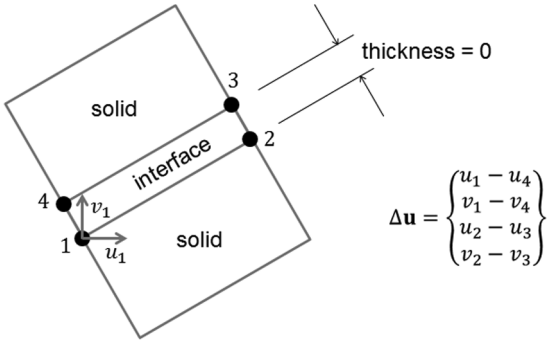

Fig. 3. Joint interface element.

where K_T is the bulk modulus of the solid skeleton.

Energy field equation:

Substituting the involved constitutive equations of water from Appendix A into Eq. (32) gives the energy field equation.

3.2. Concrete

In this study, the concrete of the pile is considered non-porous, linear elastic material. Though, it is worth mentioning that concrete is a porous material and might exhibit damage due to freezing [22,17], but the focus in this paper is on the effect of freezing on the soil mass and the pile-soil interaction.

The relevant conservation laws are the momentum and energy equations.

Momentum field equation

The momentum field equation for concrete can be expressed as

$$\nabla\cdot\left[\boldsymbol{D}_c\left(\boldsymbol{L}\boldsymbol{u} - \frac{1}{3}\boldsymbol{m}\beta_c T_c\right)\right] + \rho_c\boldsymbol{g} = 0 \tag{33}$$

where T_c is the concrete temperature, β_c is the volumetric thermal expansion coefficient, ρ_c is the mass density, and $\boldsymbol{D}_c$ is the linear elastic stiffness matrix, similar to that for soil, Eq. (8), but its elastic modulus E_c is constant (not function of temperature).

Energy field equation

The energy field equation for concrete can be expressed as

$$\rho_c c_c\frac{\partial T_c}{\partial t} + \nabla\cdot(-\boldsymbol{\lambda}_c\cdot\nabla T_c) = 0 \tag{34}$$

where c_c denotes the specific heat capacity of concrete, and λ_c is its thermal conductivity.

3.3. Heat exchanger

The heat exchanger is considered a 1D, non-deforming conductive-convective heat source. It is governed only by the energy equation.

Energy field equation

The energy field equation of the heat exchanger is expressed as

$$\rho_r c_r\frac{\partial T_r}{\partial t} - \lambda_r\frac{\partial^2 T_r}{\partial s^2} + \rho_r c_r v_r\frac{\partial T_r}{\partial s} = b_{cr}(T_r - T_c) \tag{35}$$

where T_r, ρ_r, c_r, λ_r, and v_r denote the temperature, mass density, specific heat capacity, thermal conductivity, and velocity of the circulating fluid, respectively, and b_{cr} is the thermal interaction coefficient between the circulating fluid and concrete, described in Appendix B. It is worth noting that the inclusion of the thermal interaction term in the differential equation allows embedding the heat exchanger element in the 3D concrete element.

3.4. Pile–soil interface

Accurate estimate of the load–deformation behavior of the pile–soil interface is essential for determining the integrity of the interaction between the pile and the soil. Most current numerical models for pile–soil interaction use interface elements based on the joint element, first introduced by Goodman et al. [36]. This element is of zero thickness, and formulated based on the relative displacements of solid elements surrounding the interface, Fig. 3. It is expressed in terms of stress-displacement relationship, as

$$\{\mathrm{d}\boldsymbol{\sigma}\} = [\boldsymbol{C}]\{\mathrm{d}\Delta\boldsymbol{u}\} \tag{36}$$

in which $\mathrm{d}\sigma$ is the incremental stress, $\boldsymbol{C}$ is the stiffness matrix and $\mathrm{d}\Delta\mathbf{u}$ is the increment of the relative displacements between the two sides of the interface.

This kind of elements can describe slip/no-slip conditions at the boundary between solid elements. They are basically suitable for piles with mainly axial loading and exhibiting nearly no volume deformation at the interface with the soil mass. However, for energy piles, the induced thermo-mechanical forces give rise to thermal expansion and contraction in and around the pile, leading to changes in volume. Furthermore, cyclic thermal loading can lead to slip, debonding and rebonding at the pile–soil interface. The volume change becomes more significant with thermal loads leading to cycles of freezing and thawing. Hence, for energy piles, it is more appropriate to utilize a solid element which exhibits volume change. This kind of elements was first proposed by Zienkiewicz et al. [37] who utilized an isoparametric finite element to model the interface of jointed rock systems. Based on this, Desai et al. [11] introduced a thin-layer element for modeling interfaces with different deformation modes, including slip, no-slip, debonding and rebonding. This element describes the soil at the interface as a homogeneous solid matrix. Here, we extend this element to a multiphase porous mixture.

The thin-layer element is basically formulated similar to the solid elements, and its constitutive relationship is expressed in the usual stress-strain space, as

$$\{\mathrm{d}\boldsymbol{\sigma}\} = [\boldsymbol{C}]\{\mathrm{d}\varepsilon\} \tag{37}$$

Similar to the soil momentum balance equations, Eqs. (5) and (6), the momentum balance equation for the thin-layer interface can be expressed as

$$\nabla\cdot\left[\boldsymbol{C}^{ep}\left(\boldsymbol{L}\mathrm{d}\boldsymbol{u} - \frac{1}{3}\boldsymbol{m}\beta_i\mathrm{d}T_i\right) - \boldsymbol{m}\alpha\left(\frac{\partial p_s}{\partial h_m}\mathrm{d}h_m + \frac{\partial p_s}{\partial p_m}\mathrm{d}p_m + \frac{\partial p_s}{\partial s_c}\mathrm{d}s_c\right)\right] + \left(\frac{\partial\rho^i_{eff}}{\partial h_m}\mathrm{d}h_m + \frac{\partial\rho^i_{eff}}{\partial p_m}\mathrm{d}p_m\right)\boldsymbol{g} = 0 \tag{38}$$

in which $\boldsymbol{C}^{ep}$ is the elastoplastic stiffness matrix of the interface material, β_i is the volumetric thermal expansion coefficient, T_i is the interface temperature, and ρ^i_{eff} is the effective mass density, defined as

$$\rho^i_{eff} = (1-\varphi_i)\rho_{si} + \varphi_i S_{ice}\rho_{ice} + \varphi_i S_{lw}\rho_{lw} \tag{39}$$

where φ_i is the porosity of the interface, and ρ_{si} is the mass density of the interface solid matrix. The porosity change of the soil at the interface is governed by Eq. (18).

The stiffness matrix, $\boldsymbol{C}^{ep}$, is described in Eq. (7) with an associated yield and potential functions, F_i, governed by the Drucker-Prager elastoplastic criterion:

$$F_i = q - p\tan\phi - c = 0 \tag{40}$$

where ϕ is the friction angle and c is the cohesion, described as [26]

$$c = c_0 e^{\frac{1}{n_i}(\varepsilon^p_v - \varepsilon^p_{v0})} \tag{41}$$

in which c_0 is the initial cohesion and n_i is an empirical constant for

hardening or softening. The consistency condition of the Drucker-Prager yield surface is as given in Eq. (12), with its derivatives:

$$\frac{\partial F}{\partial \boldsymbol{\sigma}'} = \frac{\tan\phi}{3}\begin{bmatrix}1\\1\\1\\0\\0\\0\end{bmatrix} + \frac{1}{2q}\begin{bmatrix}2\sigma'_x-\sigma'_y-\sigma'_z\\2\sigma'_y-\sigma'_z-\sigma'_x\\2\sigma'_z-\sigma'_x-\sigma'_y\\6\tau_{xy}\\6\tau_{yz}\\6\tau_{zx}\end{bmatrix}$$
$$\frac{\partial F}{\partial \varepsilon^p} = \frac{c}{n_i}\begin{bmatrix}1\\1\\1\\0\\0\\0\end{bmatrix} \tag{42}$$

3.5. Initial and boundary conditions

At $t = 0$, the primary state variables are described by their initial values, as

$$g(\boldsymbol{x}, 0) = g_0(\boldsymbol{x}) \tag{43}$$

where $g(\mathbf{x}, 0)$ can be any of the primary state variables $\boldsymbol{u}$, p_m, h_m, h_s, T_s, T_c, T_r, or s_c, and $g_0(\mathbf{x})$ is their initial values.

The Dirichlet boundary conditions are expressed as

$$g(\boldsymbol{x}, t) = \hat{g}(\boldsymbol{x}, t) \quad \text{on } \Gamma_u \tag{44}$$

where $\hat{g}$ denotes the prescribed values of the state variables at their relevant boundary locations, Γ_u.

The Neumann boundary conditions are expressed as:

Soil mass:

$$\begin{aligned}&\hat{\boldsymbol{t}} = \boldsymbol{\sigma}\cdot\boldsymbol{n}\\ &\hat{q}_{lw} = \rho_{lw}\boldsymbol{v}_{lw}\cdot\boldsymbol{n} \qquad \text{on } \Gamma_q\\ &\hat{Q}_{\text{soil - air}} = b_{sa}(T_s - \hat{T}_{\text{air}})\end{aligned} \tag{45}$$

where Γ_q is the Neumann boundary; $\hat{\mathbf{t}}$ is a prescribed traction; $\hat{q}_{lw}$ is a prescribed mass flow rate of liquid water; and $\hat{Q}_{\text{soil}-\text{air}}$ is the convective heat transfer between the ground surface and air, with $\hat{T}_{\text{air}}$ the air temperature, and b_{sa} the associated thermal interaction coefficient, given in Appendix B.

Pile:

$$\begin{aligned}&\hat{\boldsymbol{t}} = \boldsymbol{\sigma}\cdot\boldsymbol{n}\\ &\hat{Q}_{\text{cond}} = -\boldsymbol{\lambda}_c\nabla T_c\cdot\boldsymbol{n}\end{aligned} \qquad \text{on } \Gamma_q \tag{46}$$

Pile–heat exchanger:

$$Q^{cr} = -Q^{rc} = b_{cr}(T_c - T_r) \tag{47}$$

where b_{cr} is the thermal interaction coefficient between the heat exchanger and the pile concrete, given in Appendix B. This equation indicates that this heat flux is equal in magnitude and opposite in direction to Q^{rc} (right-hand side of Eq. (35)).

Pile–soil:

$$Q^{cs} = -Q^{sc} = b_{sc}(T_c - T_s) \tag{48}$$

in which Q^{cs} is the heat transfer between the soil and concrete pile, with b_{sc} the associated thermal interaction coefficient, given in Appendix B.

4. Finite element discretization

The governing equations are linearized using the modified Newton-Raphson method and discretized using the Galerkin finite element method. The linearization and discretization procedures are given in detail in Arzanfudi and Al-Khoury [5]. Here, we present the finite element equation, tailored to the energy pile system, and we discuss in detail the discretization of the embedded 1D element for the heat exchanger.

The global finite element equation for the energy pile can, symbolically, be described as

$$\begin{bmatrix}[\boldsymbol{C}]^s_{11}+[\boldsymbol{C}]^l_{11}+[\boldsymbol{C}]^c_{11} & [\boldsymbol{C}]^s_{12}+[\boldsymbol{C}]^l_{12} & [\boldsymbol{C}]^s_{13}+[\boldsymbol{C}]^l_{13} & [\boldsymbol{C}]^s_{14}+[\boldsymbol{C}]^l_{14} & [\boldsymbol{C}]^s_{15}+[\boldsymbol{C}]^l_{15} & [\boldsymbol{C}]^c_{16}+[\boldsymbol{C}]^l_{16} & 0\\ [\boldsymbol{C}]^s_{21}+[\boldsymbol{C}]^l_{21} & [\boldsymbol{C}]^s_{22}+[\boldsymbol{C}]^l_{22} & [\boldsymbol{C}]^s_{23}+[\boldsymbol{C}]^l_{23} & [\boldsymbol{C}]^s_{24}+[\boldsymbol{C}]^l_{24} & [\boldsymbol{C}]^s_{25}+[\boldsymbol{C}]^l_{25} & 0 & 0\\ [\boldsymbol{C}]^s_{31} & [\boldsymbol{C}]^s_{32} & [\boldsymbol{C}]^s_{33} & [\boldsymbol{C}]^s_{34} & [\boldsymbol{C}]^s_{35} & 0 & 0\\ 0 & 0 & 0 & 0 & 0 & 0 & 0\\ 0 & 0 & 0 & 0 & 0 & 0 & 0\\ 0 & 0 & 0 & 0 & 0 & [\boldsymbol{C}]^c_{66} & 0\\ 0 & 0 & 0 & 0 & 0 & 0 & [\boldsymbol{C}]^r_{77}\end{bmatrix}\begin{bmatrix}\{\dot{\tilde{\boldsymbol{u}}}\}\\ \{\dot{\tilde{\boldsymbol{p}}}_m\}\\ \{\dot{\tilde{\boldsymbol{h}}}_m\}\\ \{\dot{\tilde{\boldsymbol{T}}}_s\}\\ \{\dot{\tilde{\boldsymbol{s}}}_c\}\\ \{\dot{\tilde{\boldsymbol{T}}}_c\}\\ \{\dot{\tilde{\boldsymbol{T}}}_r\}\end{bmatrix}$$
$$+\begin{bmatrix}0 & 0 & 0 & 0 & 0 & 0 & 0\\ 0 & [\boldsymbol{K}]^s_{22}+[\boldsymbol{K}]^l_{22} & 0 & 0 & [\boldsymbol{K}]^s_{25}+[\boldsymbol{K}]^l_{25} & 0 & 0\\ 0 & [\boldsymbol{K}]^s_{32} & 0 & [\boldsymbol{K}]^s_{34} & [\boldsymbol{K}]^s_{35} & 0 & 0\\ 0 & 0 & 0 & [\boldsymbol{K}]^s_{44} & 0 & 0 & 0\\ 0 & 0 & 0 & 0 & [\boldsymbol{K}]^s_{55} & 0 & 0\\ 0 & 0 & 0 & 0 & 0 & [\boldsymbol{K}]^c_{66} & 0\\ 0 & 0 & 0 & 0 & 0 & 0 & [\boldsymbol{K}]^r_{77}\end{bmatrix}\begin{bmatrix}\{\tilde{\boldsymbol{u}}\}\\ \{\tilde{\boldsymbol{p}}_m\}\\ \{\tilde{\boldsymbol{h}}_m\}\\ \{\tilde{\boldsymbol{T}}_s\}\\ \{\tilde{\boldsymbol{s}}_c\}\\ \{\tilde{\boldsymbol{T}}_c\}\\ \{\tilde{\boldsymbol{T}}_r\}\end{bmatrix}$$
$$=\begin{bmatrix}\{\boldsymbol{f}^s_1\}+\{\boldsymbol{f}^c_1\}\\ \{\boldsymbol{f}^s_2\}\\ \{\boldsymbol{f}^s_3\}+\{\boldsymbol{f}^{sc}\}\\ \{\boldsymbol{f}^s_4\}\\ \{\boldsymbol{f}^s_5\}\\ \{\boldsymbol{f}^c_6\}+\{\boldsymbol{f}^{cs}\}+\{\boldsymbol{f}^{cr}\}\\ \{\boldsymbol{f}^{rc}\}\end{bmatrix} \tag{49}$$

where the subscripts/superscripts s, c, i denote the soil matrix, concrete and interface, respectively, and the subscripts m, r represent the pore water mixture and circulating water, respectively. The vector on the right-hand side represents the THM force vector, including heat fluxes

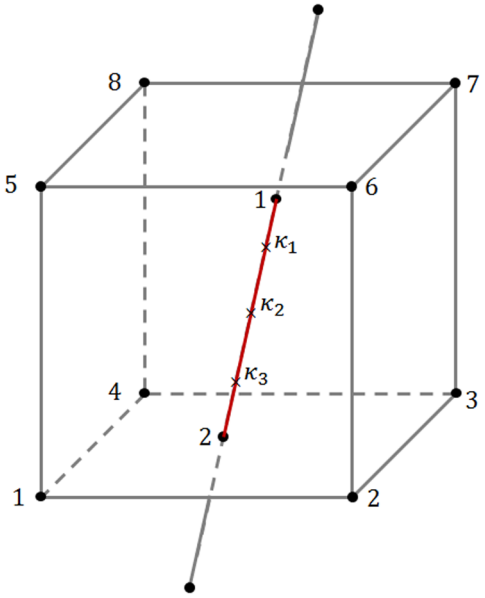

Fig. 4. Embedded 1D element in a host 3D element.

due to the thermal interactions at the interface boundaries between the heat exchanger, pile and soil mass. The matrix entries of Eq. (49) represent 3D and 1D element matrices, expressed hereafter.

4.1. 3D element

The matrix and vector entries for 3D soil, concrete and interface elements, including $\boldsymbol{C}^s_{ij}$, $\boldsymbol{K}^s_{ij}$, $\boldsymbol{f}^s_i$, $\boldsymbol{C}^c_{ij}$, $\boldsymbol{K}^c_{ij}$, $\boldsymbol{f}^c_i$, $\boldsymbol{f}^{cs}_i$, $\boldsymbol{f}^{sc}_i$, $\boldsymbol{C}^i_{ij}$ and $\boldsymbol{K}^i_{ij}$, are given in Appendix D.

4.2. Embedded 1D element

The heat exchanger is discretized using a linear embedded 1D element. This element can go through the host 3D elements without affecting the underlying structure of the mesh, Fig. 4. The essence of this kind of elements is that the host and embedded elements are discretized in the usual manner, except for their interaction terms; $\boldsymbol{f}^{cr}$ and $\boldsymbol{f}^{rc}$ (Eq. (49)). This enables a simpler discretization of the problem.

The finite element terms of the host concrete element, $\boldsymbol{K}^c_{ij}$, $\boldsymbol{C}^c_{ij}$, and $\boldsymbol{f}^c_i$, are given in Eq. (D.2). The finite element terms for the embedded heat exchanger element, $\boldsymbol{K}^r_{77}$, $\boldsymbol{C}^r_{77}$ in Eq. (49), can readily be derived by applying the Galerkin method to the left-hand side of Eq. (35), leading to

$$\begin{aligned}\boldsymbol{K}^r_{77} &= \int_V (\boldsymbol{B}^T_e \lambda_r \boldsymbol{B}_e + \boldsymbol{N}^T_e \rho_r c_r v_r \boldsymbol{B}_e) dV \\ \boldsymbol{C}^r_{77} &= \int_V \boldsymbol{N}^T_e \rho_r c_r \boldsymbol{N}_e dV\end{aligned} \tag{50}$$

where the subscript e stands for the embedded element, $\boldsymbol{B}_e = \nabla \boldsymbol{N}_e$, and V is the volume of the heat exchanger.

Applying the weighted residual method to the thermal interaction forces, $\boldsymbol{f}^{cr}$ and $\boldsymbol{f}^{rc}$, Eq. (47), yields

$$\begin{aligned}\boldsymbol{f}^{cr} &= \int_S w\, Q^{cr} dS \\ \boldsymbol{f}^{rc} &= -\int_S w_e Q^{cr} dS\end{aligned} \tag{51}$$

in which S is the surface area of the heat exchanger, $w = \boldsymbol{N}(\boldsymbol{x})$ and $w_e = \boldsymbol{N}_e(\boldsymbol{x})$ are the finite element weighting functions for the host element and embedded element, respectively, and Q^{cr} is the coupling term between the two elements, Eq. (47), expressed as

$$Q^{cr}(\boldsymbol{x}, s, t) \equiv \boldsymbol{N}_{eh}(\boldsymbol{x}, s)\overline{\boldsymbol{Q}}^{cr}(t) \tag{52}$$

in which

$$\begin{aligned}\boldsymbol{N}_{eh}(\boldsymbol{x}, s) &= [\boldsymbol{N}(\boldsymbol{x}) \quad | \quad -\boldsymbol{N}_e(\boldsymbol{x})] \\ \bar{\boldsymbol{Q}}^{cr}(t) &= b_{cr}[\bar{\boldsymbol{T}}_c(t) \quad | \quad \bar{\boldsymbol{T}}_r(t)]^T\end{aligned} \tag{53}$$

where $\boldsymbol{N}_{eh}$ is embedded–host coupled shape function. For a two-node 1D element embedded in an 8-node 3D element, Fig. 4, using the Gauss quadrature, Eq. (51) can be expressed as

$$\begin{aligned}\boldsymbol{f}^{cr} &= 2\pi r_i\, b_{cr} \sum_{\kappa=1}^{n} w_\kappa \begin{Bmatrix} N_1(\boldsymbol{x}_\kappa) \\ \vdots \\ N_8(\boldsymbol{x}_\kappa) \end{Bmatrix} \cdot \begin{Bmatrix} N_1(\boldsymbol{x}_\kappa) \\ \vdots \\ N_8(\boldsymbol{x}_\kappa) \\ -N_{e1}(\boldsymbol{x}_\kappa) \\ -N_{e2}(\boldsymbol{x}_\kappa) \end{Bmatrix}^T \cdot \begin{Bmatrix} T_1 \\ \vdots \\ T_8 \\ T_{r1} \\ T_{r2} \end{Bmatrix} \\ \boldsymbol{f}^{rc} &= -2\pi r_i\, b_{cr} \sum_{\kappa=1}^{n} w_\kappa \begin{Bmatrix} N_{e1}(\boldsymbol{x}_\kappa) \\ N_{e2}(\boldsymbol{x}_\kappa) \end{Bmatrix} \cdot \begin{Bmatrix} N_1(\boldsymbol{x}_\kappa) \\ \vdots \\ N_8(\boldsymbol{x}_\kappa) \\ -N_{e1}(\boldsymbol{x}_\kappa) \\ -N_{e2}(\boldsymbol{x}_\kappa) \end{Bmatrix}^T \cdot \begin{Bmatrix} T_1 \\ \vdots \\ T_8 \\ T_{r1} \\ T_{r2} \end{Bmatrix}\end{aligned} \tag{54}$$

where n is the number of Gaussian integration points in the 1D element ($n = 3$ in Fig. 4), w_k is the Gaussian quadrature weight, and $N_j(\boldsymbol{x}_\kappa)$; $j = 1, \cdots, 8$ and $N_{ej}(\boldsymbol{x}_\kappa)$; $j = 1, 2$ are the weighting and shape functions of the host and embedded elements at sampling point κ, respectively.

5. Model verification against London energy pile experiment

There are relatively few well-documented full-scale energy pile experiments in the literature. Here, the results of the well-known London energy pile experiment presented by Bourne-Webb et al. [7], and Amatya et al. [2] are utilized to verify the proposed model.

5.1. Physical domain

The London energy pile experiment is conducted using a single energy pile, 23 m in length, in which a double U-tube heat exchanger is embedded. The lower 18 m of the pile is 0.55 m in diameter, and the

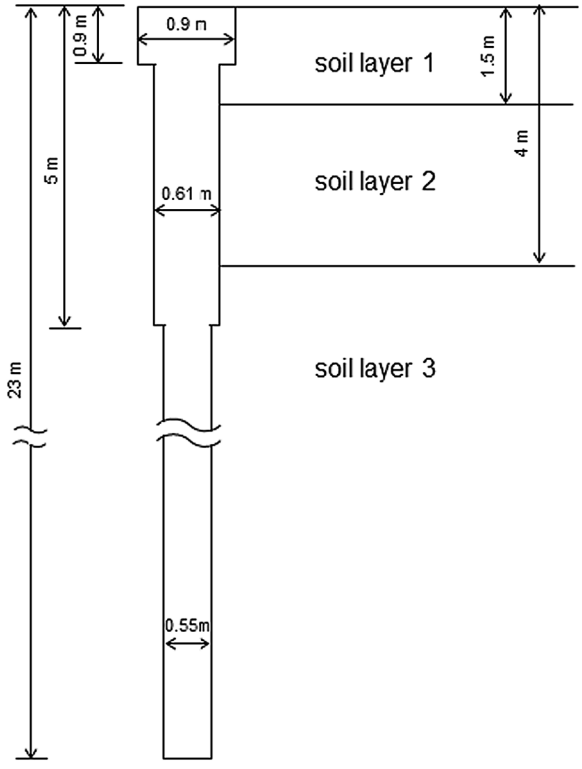

Fig. 5. London energy pile geometry.

Table 1
Material properties.

	Soil Layer 1	Soil Layer 2	Soil Layer 3	Concrete	Interface	Circulating fluid	Pipe material	Air
Depth (m):	0 – 1.5	1.5 – 4	>4	–	–	–	–	–
Mechanical:								
ρ (kg m^{-3})	1940	2040	2040	2550	1940	1052	–	1.2466
E (MPa)	36	140	70	40,000	70	–	–	–
ν (–)	0.3	0.3	0.3	0.15	0.3	–	–	–
K_s (MPa)	500	500	500	–	–	–	–	–
b (K^{-1})	0.1	0.1	0.1	–	–	–	–	–
M_{cs} (–)	1.33	1.42	0.98	–	–	–	–	–
p_{pc0} (kPa)	700	700	700	–	–	–	–	–
Φ (°)	–	–	–	–	10	–	–	–
c (kPa)	–	–	–	–	15	–	–	–
n (–)	0.006	0.006	0.006	–	−9	–	–	–
Thermal:								
c_p (J kg^{-1} K^{-1})	1200	1200	1500	800	1200	3795	–	1006
λ (W m^{-1} K^{-1})	2	2	1.5	1.8	2	0.48	0.42	0.02572
β (10^{-6} K^{-1})	15	15	15	25.5	15	–	–	–
Hydraulic:								
μ (10^{-6} kg m$^{-1}s^{-1}$)	–	–	–	–	–	5200	–	17.6488
ν (m s^{-1})	–	–	–	–	–	0.2	–	0.16667
Porous:								
φ (–)	0.3	0.3	0.3	–	0.3	–	–	–
k (mD)	1160	1160	0.0116	–	1160	–	–	–
η (–)	7.5	7.5	7.5	–	–	–	–	–
S^* (–)	0	0	0	–	–	–	–	–
a (K^{-1})	0.03	0.03	0.03	–	–	–	–	–

upper 5 m is cased in two diameters: 0.61 m for 4.1 m and 0.9 m for 0.9 m, Fig. 5. The configuration of the U-tubes inside the pile is shown in Fig. 1a. The energy pile is embedded in a soil mass consisting of three layers: 1.5 m of made ground, 2.5 m of sandy gravel, and the rest is London clay. The physical and thermal parameters of the system are given in Table 1.

5.2. Initial and boundary conditions

Initially, the temperature in the domain, as reported in Bourne-Webb et al. [7], is 19.5 °C.

Mechanical boundary condition: The pile is subjected to two mechanical vertical loading/unloading forces: 1200 kN and 1800 kN.

Thermal boundary conditions: The system is subjected to 31 days of cooling, followed by 12 days of heating. Fig. 6 shows the input temperature which ranges between −6°C and 40 °C, applied at the inlet of the U-tube. According to the literature of this experiment, a power failure occurred after 36 days and lasted for 4 days.

5.3. Computational domain

The physical processes in the system are three-dimensional, but the geometry is planar symmetric with respect to the plane that passes through the middle of the pile, Fig. 7. Accordingly, only half of the geometry is considered. The computational domain is 100 m in diameter and 70 m in depth, divided into three soil layers resembling made ground, sandy gravel and London clay (Table 1). An energy concrete pile, embedded in which double U-tubes, is located at the axis of symmetry.

The mesh consists of 1548, 3D linear hexahedron and wedge-shaped elements for the pile and the soil mass; 84, 3D hexahedron elements for the pile–soil interface; and 26, embedded 1D linear finite elements for the heat exchanger. The thickness of interface is 0.02 m. A view of the finite element mesh at the proximity of the pile is given in Fig. 7.

The prescribed initial and boundary conditions are:

Initial conditions:

$T_{s0} = T_{c0} = T_{r0} = 19.5$ °C

$p_{c0} = 700$ kPa

$p_{lw0} = p|_{hydrostatic} = -\rho_{lw0} g z$

$\sigma'_{z0} = \rho_s g z + p_{lw0}$

where z is the depth.

Boundary conditions:

Thermal boundary conditions:

$\hat{T}_{air} = 19.5$ °C

$\hat{T}_s|_{bottom} = 19.5$ °C

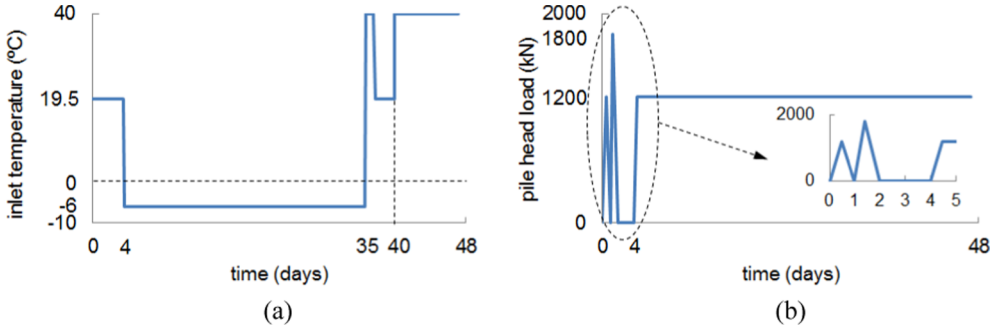

Fig. 6. Boundary conditions: (a) Heat exchanger input temperature, (b) Pile head mechanical load.

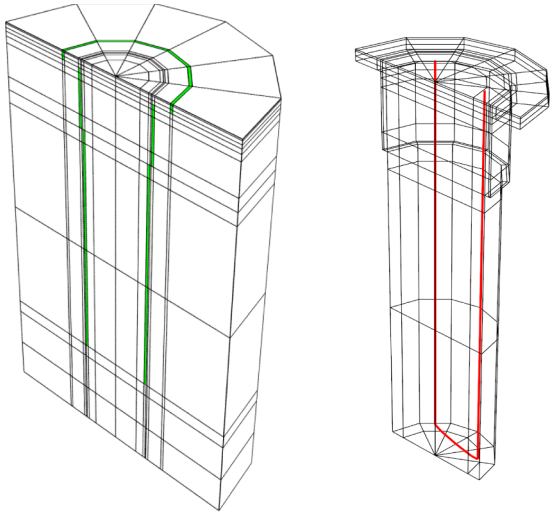

(a) (b)

Fig. 7. Finite element mesh in the proximity of the pile (scale 10:1 in radial direction): (a) pile, thin-layer interface (green) and surrounding soil, and (b) embedded heat exchanger elements (red). (For interpretation of the references to colour in this figure legend, the reader is referred to the web version of this article.)

$\hat{T}_r|_{inlet}$=varying, see Fig. 6a
where the ground surface heat flow is prescribed based on Eq. (45) with $b_{sa} = 0.6\ \ W\ \ m^{-2}\ \ K^{-1}$.
Hydraulic boundary conditions:
Top/side boundaries: drained
Bottom boundary: undrained
Mechanical boundary conditions:
$F|_{pilehead}$=varying, see Fig. 6b
Top boundary: no constraints (free to move)
Bottom boundary: fully constrained
Side boundaries: horizontally constrained

5.4. Experiment-computation comparison

The computed and measured temperatures are compared at a point in the pile 9 m below the surface and 0.2 m from the axis of symmetry; and two points in the soil mass 9 m in depth, and 0.5 m and 2 m radially. The angular coordinates of the sensors are not indicated in the literatures, and hence, the computational results are presented at five angular positions, $\theta = 0^{\circ}, 45^{\circ}, 90^{\circ}, 135^{\circ}$, and$180^{\circ}$, Fig. 8a.

Fig. 8b shows the measured and computed temperatures in the pile, and Fig. 8c and Fig. 8d show those in the soil mass. In general, the figures display a good match between the two results. Though, due to power failure at time, $t = 36 - 40$days, there is some mismatch between the computed and measured data in the pile. The power failure has been modeled as switching off of the heat pump (see Fig. 6), but the exact consequences of this failure on the measurement devices are not clear. Therefore, the comparison is not reliable in this period.

Fig. 9 shows the computed thermo-mechanical pile head displacement as compared to the measured data. The figure shows a good match between the two results, especially before the power failure.

Fig. 10 shows the computed mechanical and thermo-mechanical axial strain along the pile, together with the measured data. Fig. 10a shows that there is a good agreement in the axial strain due to mechanical loading. Fig. 10b displays the thermal strain at the end of cooling ($t = 35$ days). This figure shows a reasonable matching between the computed and measured results, though, there is some deviation between the two results, which might be attributed to the mobilization of the pile–soil interface due to the thermal contraction of the

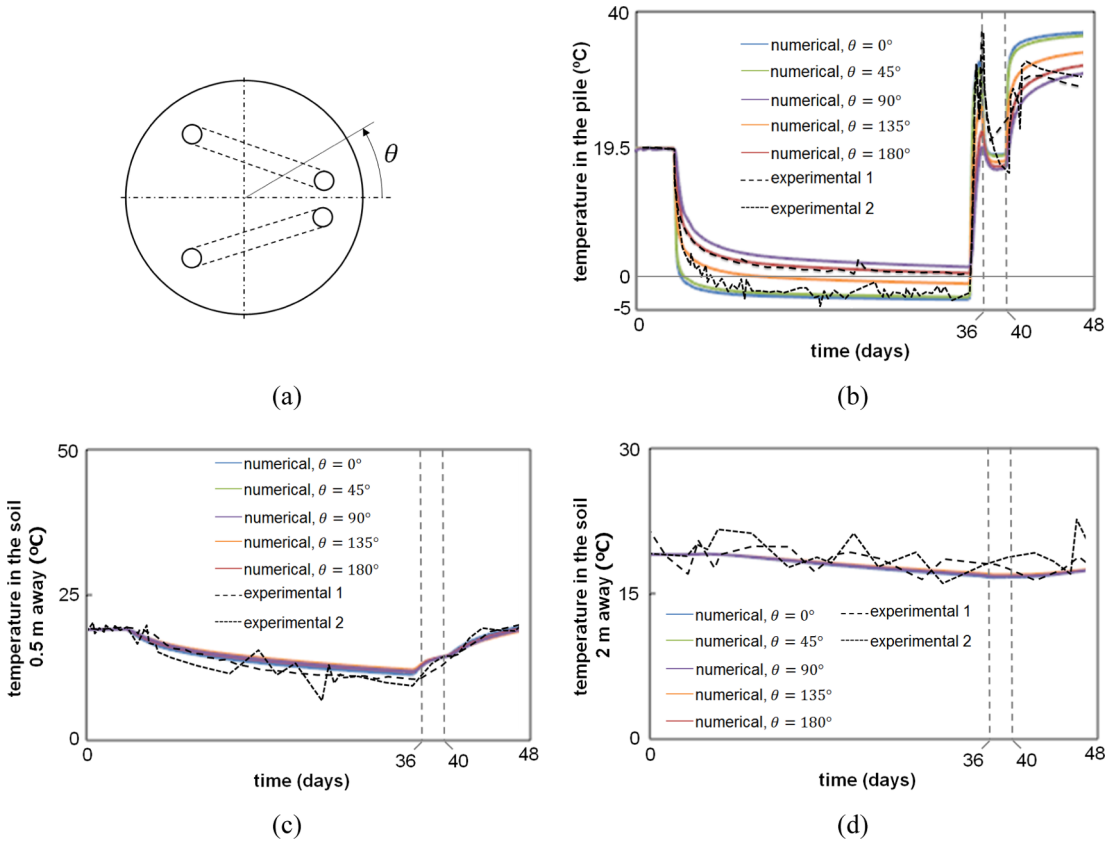

Fig. 8. Computed and experimental evolution of temperatures, 9 m below the surface: (a) angular indicator of inspected points; (b) energy pile; (c) soil, 0.5 m away from pile; (d) soil, 2 m away from pile.

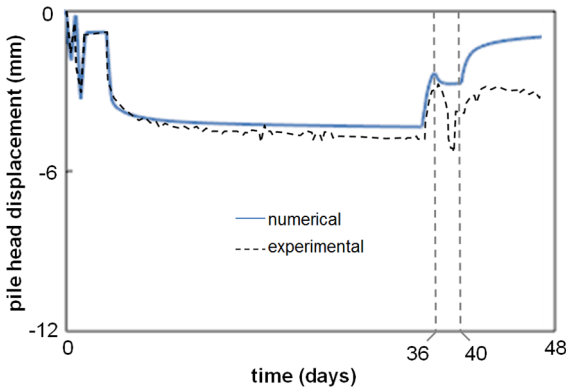

Fig. 9. Computed and experimental evolution of pile head vertical displacement.

concrete and soil. The behavior of the pile–soil interface of the London energy pile is not reported in the literature.

Fig. 10c shows the strain at the end of heating ($t = 47$ days). Even though the computed results are not matching the measured data, they exhibit a similar trend. The mismatch can be attributed to the power failure and the uncertainty at the pile–soil interface. Other literatures reveal a similar mismatch, see [35,16,3].

It is worth mentioning that the observed reversibility in the axial strain in Fig. 10 occurs due to a combination between the reversibility of the elastic strain and the change of stress direction between the heating mode and the cooling mode. However, its magnitude is influenced by the configuration of the heat pipes inside the pile and their temperature gradient along the pile; the pile-soil interaction; and the type of the surrounding soil mass and its mechanical, thermal and hydraulic properties. Therefore, detailed description of the physics is of paramount importance to describe the behaviour of energy pile systems. Mimouni and Laloui [27] and Rotta Loria and Laloui [31], among others, highlighted the issue of reversibility of the axial and radial strains in energy piles.

6. Numerical energy pile experiment

The verification example given in the previous section indicates that the proposed multiphase thermo-hydro-mechanical modeling approach can provide reasonably accurate computational results describing the behavior of typical energy pile set-ups. However, this is not exceptional as many other computational approaches, including Yavari et al. [35], Di Donna and Laloui [12], Gawecka et al. [16], and Anongphouth et al. [3], are capable of simulating full-scale experiments to a practically accepted level of accuracy. This is feasible since the boundary conditions adopted in most full-scale experiments are restrained to a limited range. The heating system in these experiments is usually operated with relatively low heat extraction rates to make sure that the soil does not freeze. This makes the simulation of the thermo-hydro-mechanical processes feasible via standard constitutive models and numerical discretization procedures. However, in practice, such a constraint can lead to limiting the energy efficiency of the system in at least two important engineering scenarios:

1. Limiting the operation of the system to relatively low circulating flow rates would lead to low heat harvest, and
2. Limiting the system operation to above freezing level would lead to shorter operation time, and hence less efficiency.

The proposed model, on the other hand, is designed to simulate conditions that go beyond the current operation constraints to allow for higher energy extractions and longer periods of operation. To examine these capabilities, we extended the London energy pile experiment numerically to attain cycles of freezing and thawing conditions in the system.

6.1. Initial and boundary conditions

The initial and boundary conditions are the same as those for the verification example in Section 5, except the following:

Initial condition:

The temperature in the system is assumed 10 °C. This relatively low temperature was chosen to accelerate the freezing condition in the system.

Mechanical boundary condition:

A mechanical load of 1200 kN is applied at the pile head prior to the thermal loading.

Thermal boundary conditions:

The upper boundary of the soil mass is subjected to a constant air temperature of 10 °C, and the bottom boundary is prescribed at 10 °C.

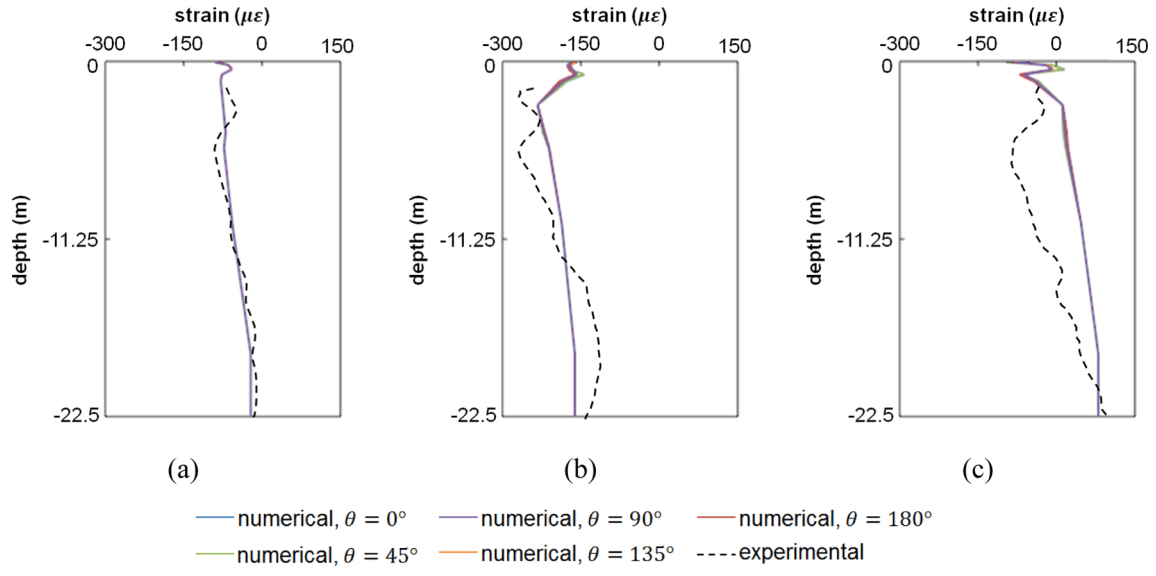

Fig. 10. Computed and experimental vertical strain along pile axis: (a) mechanical, (b) end of cooling, (c) end of heating.

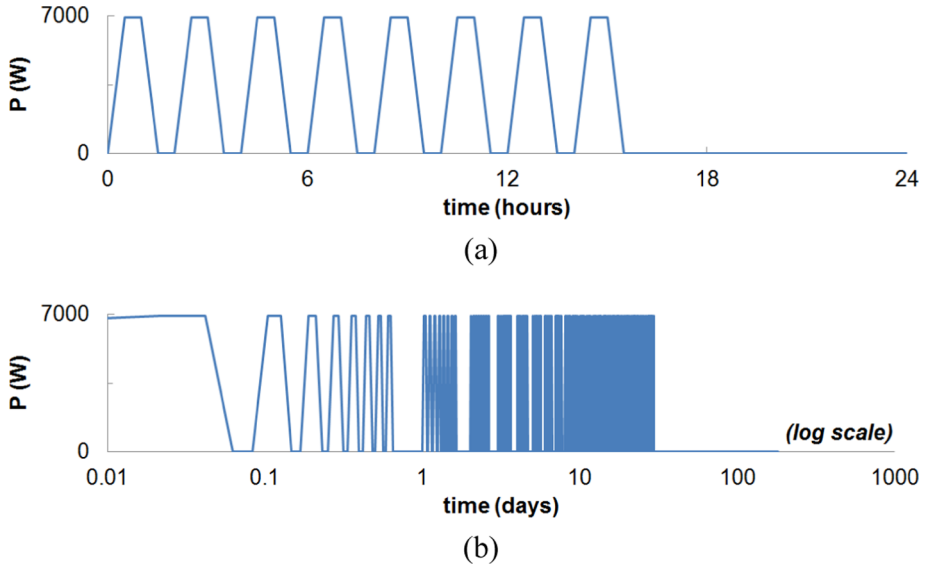

Fig. 11. Applied thermal load: (a) during a day, and (b) during 6 months.

The heat exchanger is subjected to a cyclic thermal load, ranging between 0 and 7 kW. Eight cycles of switching on and off for 2 h are applied at the inlet of the heat exchanger for 16 h, followed by 8 h switching off, Fig. 11a. The cycles are repeated for 30 days, after which the heat pump is switched off for 5 months, as shown in Fig. 11b. According to current specifications this thermal load is not realistic, but adopted to study the feasibility of using the proposed model for high energy extraction rates and cyclic freezing and thawing conditions.

The cyclic heat pump power is converted to a prescribed inlet temperature, T_{in}, utilizing the heat pump–heat exchanger set-up schematically given in Fig. 12. Depending on the HVAC design, the heat pump extracts a required amount of heat from the fluid coming out of the heat exchanger outlet, and returns it to its inlet. The amount of power extracted from the heat pump can be calculated by

$$P = \dot{m} c_r (T^{\text{p}}_{\text{out}} - T^{\text{p}}_{\text{in}}) \tag{55}$$

in which $\dot{m}$ is the mass flow rate of the circulating fluid, c_r is the specific heat capacity of the circulating fluid, T^p_{in} is the fluid temperature entering the heat pump and T^p_{out} is the fluid temperature leaving the heat pump. Ignoring the heat loss in the pipes, which carry the circulating fluid, T^p_{in} is equal to T_{out} (temperature leaving the heat exchanger); and T^p_{out} is equal to T_{in} (temperature entering the heat exchanger). Having this heat exchange set-up between the heat pump and the heat exchanger, T_{in} can be calculated from Eq. (55).

6.2. Physical and computational domains

The geometry and material parameters of the physical domain, together with the types of the finite elements and the finite element mesh size are identical to those of the verification example in Section 5.

6.3. Results and discussion

The behavior of the system is presented in terms of deformation at the head and toe of the pile, temperature at the inlet and outlet of the heat exchanger, and temperature in the soil mass, 9 m below the surface, 0.3 m in the radial direction, with angular coordinates: $\theta = 0^{\circ}, 45^{\circ}, 90^{\circ}, 135^{\circ}$, and 180°. To highlight the cyclic loading, the diagrams are presented in a semi-log format.

Fig. 13a shows the temperature variation with time in the soil. It shows that freezing starts after 14 days of operation and the temperature reaches -33 °C after 30 days. A closer look at the figure reveals that in the period between day 28 and day 30 the temperature exhibits a sudden drop. This occurs due to the accumulation of ice in the soil. Fig. 13b shows the ice volume fraction during this period. It reveals that in day 14, with the onset of freezing, the ice volume fraction in the pores was 1%. According to Eqs. (A.5) and (A.8) in Appendix A, the thermal conductivity for this water mixture is 0.56 W/m·K. However, in day 30, the ice content became 9% and the thermal conductivity of the pore water rose to 0.70 W/m·K. This increase in the thermal conductivity allows more heat to transfer between the soil and the pile leading to this drop in temperature.

Fig. 13c shows the temperature profiles at the inlet and outlet of the heat exchanger. It reveals that with this relatively large heat pump power, the temperature in the circulating fluid dropped to below 0 °C from the first day, and in 30 days the temperature dropped to nearly -20 °C. The figure also reveals that the sudden drop in temperature in the soil in the period between day 28 and 30 has been reflected on the circulating fluid.

Fig. 13d shows the pile head and toe displacements. The displacement at the head generated by the mechanical load is -2.2 mm and at the toe is -0.9 mm. Upon the start of the cyclic thermal loading, the displacement in the pile exhibits ups and downs due to the thermal expansion and contraction of concrete and its interaction with the

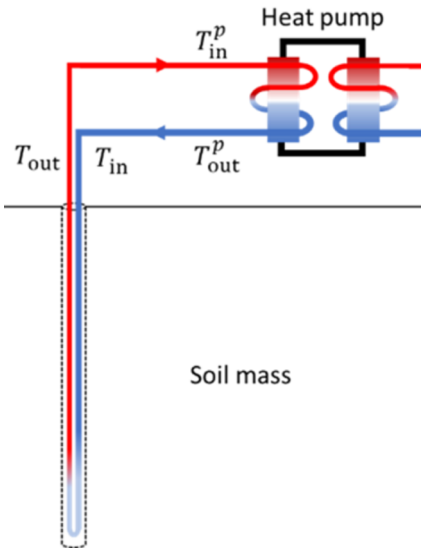

Fig. 12. Heat pump – heat exchanger set-up.

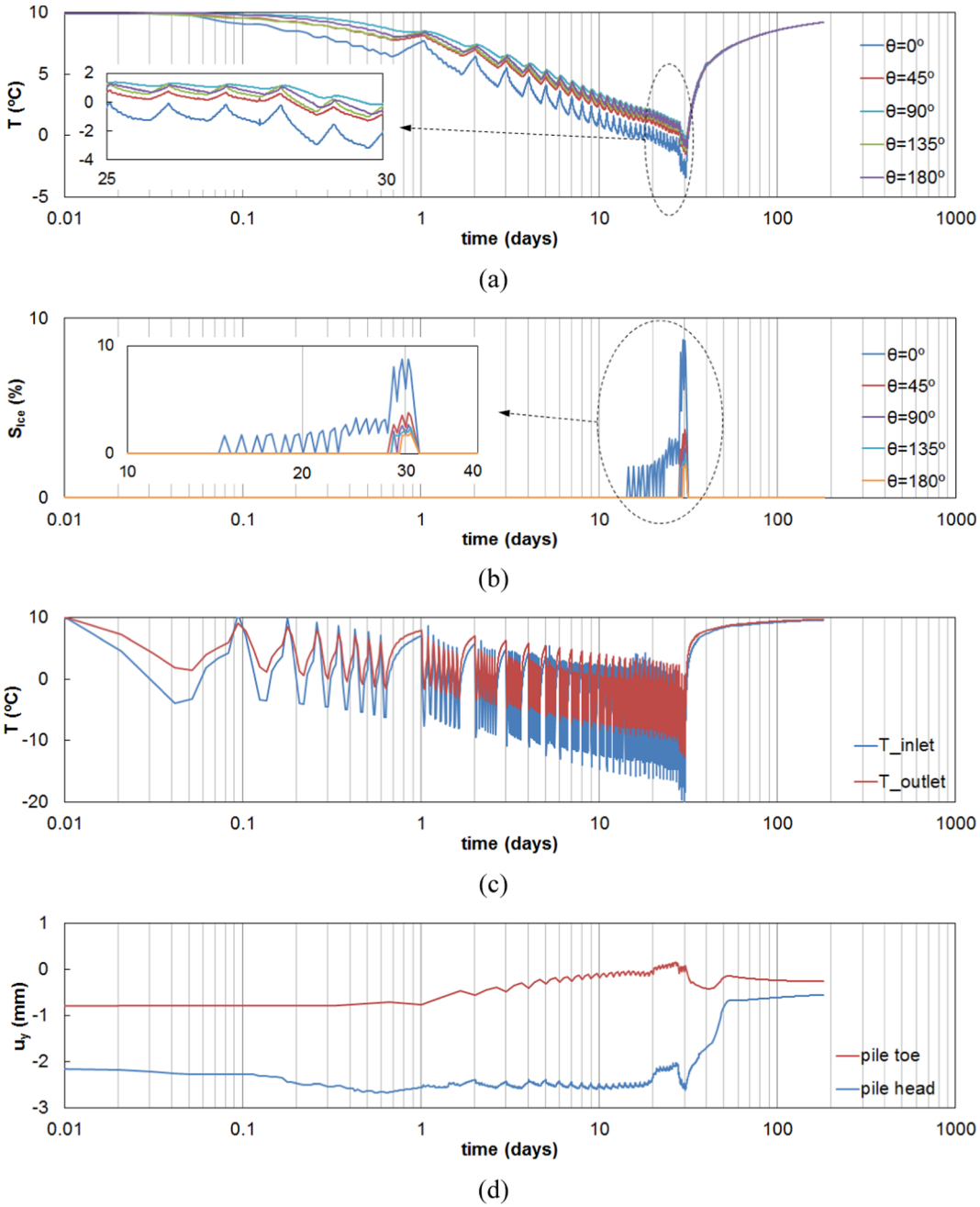

Fig. 13. Temperature, ice fraction and pile displacement: (a) temperature in soil, (b) ice fraction in soil, (c) temperature at inlet and outlet of heat exchanger, and (d) pile head and toe displacements.

surrounding soil mass. This can be clearly seen in the sketch given in Fig. 14. This figure shows the pile at its initial condition, upon the application of the mechanical load and during the thermal load cycles. The ups and downs of the pile are scaled to the amount of displacement at the head and toe of the pile, and the arrows indicate the movement direction. The following can be observed:

t = 0day: upon mechanical loading, both head and toe moved in the direction of the applied force.
t = 18days: four days after the onset of soil freezing on day 14, the pile exhibits contraction.
t = 28days: with the increase of ice content in the soil (see Fig. 13b), the pile exhibits lifting up due to the soil heave at the toe.
t = 30days: the pile temperature drops due to its thermal interaction with the heat exchanger and soil, causing the pile to contract again.
t = 40days: during thawing, the pile exhibits expansion.
t = 55days: with the increase of plastic deformation in the soil (see Fig. 15f), the soil exhibits settlement around the pile, causing the pile to lift up.
t = 180days: at the end of thawing, the pile exhibits expansion again.

Fig. 15 presents three-dimensional plots for the temperature distribution and fluid flow, the effective plastic strain, and the deformation in the proximity of the pile on day 30 (maximum freezing) and day 180 (end of thawing). Fig. 15a shows the 3D temperature distribution in the pile and the soil around it, together with the fluid flow velocity vectors. The figure shows that the concrete and approximately 0.1 m of the surrounding soil have been frozen on day 30. It also shows the water flow towards the frozen zone due to cryogenic suction. (Note that the flow pattern is not symmetric because the temperature distribution in

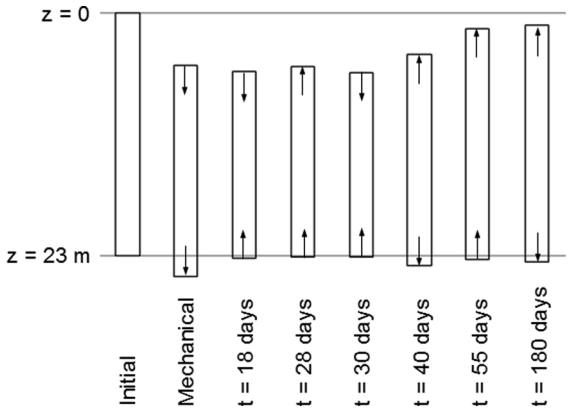

Fig. 14. Schematic presentation of pile movement (scaled).

and around the pile is not symmetric due to the unsymmetric configuration of the heat exchanger inside it (Fig. 1a). Fig. 15b reveals that upon switching off the heat pump for 5 months, the temperature in the system has recovered as a result of the heat flow between the soil mass and its boundaries.

Fig. 15c to f show the deformed mesh and their associated effective plastic strains. Fig. 15e shows that the plastic strain has already began in the first 30 days and increased considerably after thawing, Fig. 15f. This can be noticed from the deformed mesh on day 180 (Fig. 15d) as compared to day 30 (Fig. 15c). The relatively large deformation in the soil can be attributed to the fact that, upon freezing, the soil stiffness increases due to ice formation, accompanied by expansion of pores. Upon thawing, the soil stiffness reduces significantly in regions where excessive pore expansion has occurred, causing the soil above it to collapse under gravity.

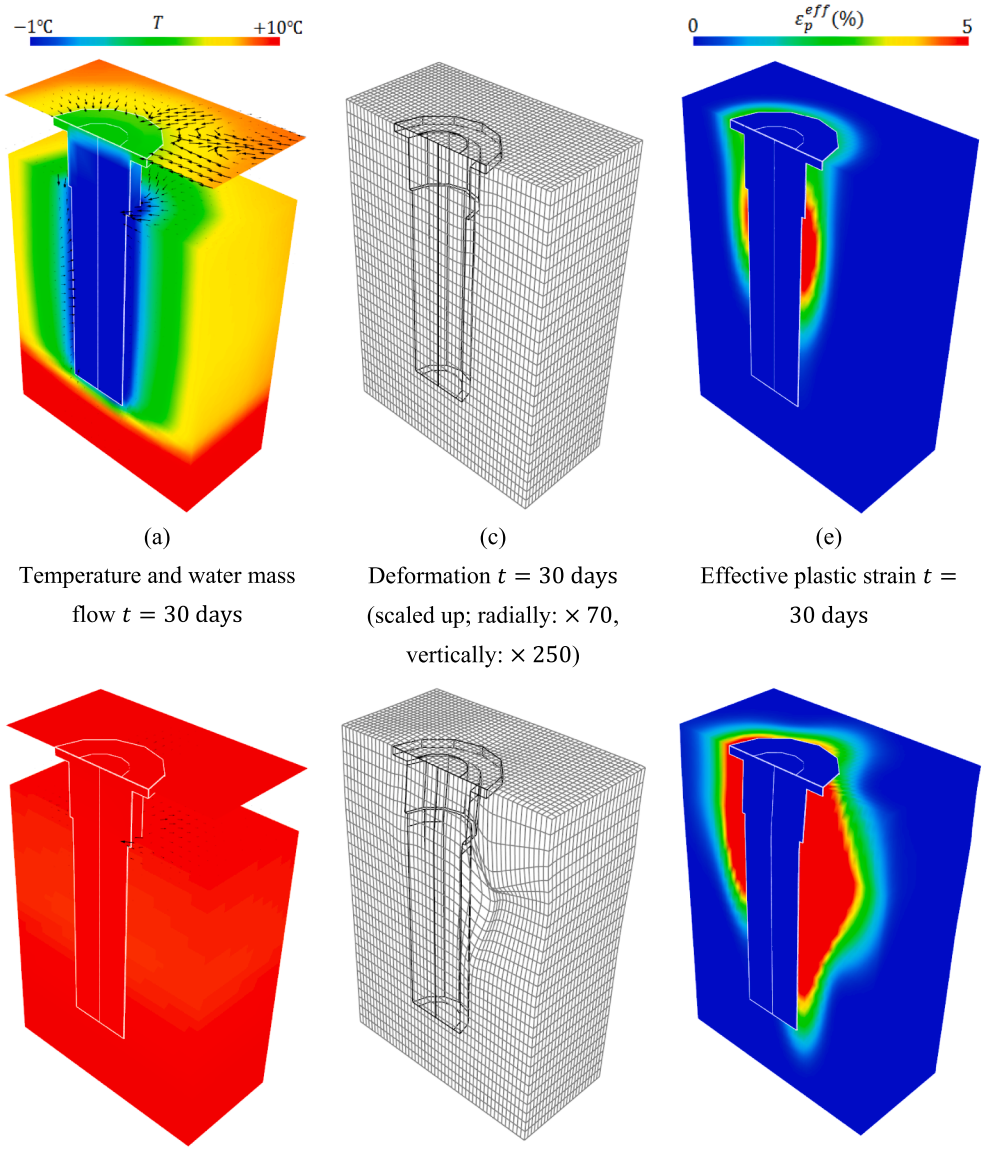

(a) Temperature and water mass flow $t = 30$ days

(c) Deformation $t = 30$ days (scaled up; radially: × 70, vertically: × 250)

(e) Effective plastic strain $t = 30$ days

(b) temperature and water mass flow $t = 180$ days

(d) Deformation $t = 180$ days (scaled up; radially: × 70, vertically: × 250)

(f) Effective plastic strain $t = 180$ days

Fig. 15. Energy pile behavior upon freezing ($t = 30$ days) and thawing ($t = 180$ days).

7. Conclusions

Current energy pile design procedures put a limit to the amount of extracted energy to make sure that operating the energy pile for heating would not lead to soil freezing. This constraint is good for safety of buildings, but short on the economy. It lessens the energy efficiency of the system because it requires low flow rates and shorter operation time. One of the reasons for this constraint is attributed to lack of understanding of the coupled thermo-hydro-mechanical forces arising from freezing and thawing of porous media and their effects on the soil properties and the pile–soil interface. Freezing and thawing in a soil mass gives rise to solid and fluid compressibility, fluid and heat flow, thermo-elastoplasticity, buoyancy, phase change, volume change, pore expansion, melting point depression, cryogenic suction and permeability reduction due to ice formation. None of the existing numerical tools used for energy piles design and analysis is capable of capturing the coupling of these processes. This paper addresses this issue and demonstrates that the proposed model is capable of capturing these processes and their coupling effects on the integrity of the energy pile systems.

The paper addresses four particular features pertaining to the physics of energy piles: three-dimensionality, embedded heat exchangers, soil constitutive modeling and pile–soil interface. It highlights several aspects related to the physics of energy piles and their operation that need to be considered in energy pile design.

1. A concrete pile exhibits deformation and movement under cyclic thermal loading with magnitudes related to its thermo-mechanical properties and the thermo-hydro-mechanical properties of the pile–soil interface and the soil mass. Fig. 14 clearly illustrates how the pile can expand and contract locally or move as a rigid body during cyclic thermal loads, leading ultimately to deteriorating the integrity of the pile–soil interaction. This signifies the fact that the thermo-hydro-mechanical properties of the system can alter during daily and seasonal operation of the energy pile, requiring special attention during design.
2. Freezing in soil leads to pore expansion which, upon thawing, might lead to weakening the strength of the pile–soil interface. Fig. 15d shows how the thawing has led to weakening part of the interface that caused the collapse of the soil above it. This emphasizes the need of taking the likely occurrence of freezing and thawing into consideration during the design. Even if current design procedures prohibit reaching to the freezing point, freezing might occur due to malfunctioning in the mechanical parts, misuse of the system or unexpected change in weather.
3. Heat conduction-convection in the heat exchanger gives rise to axial and unsymmetrical radial thermal strain gradients in the pile and the surrounding soil mass. The numerical experiment has shown that such gradients can lead to localized damage that can affect the pile–soil shaft integrity. This effect cannot be captured by the line heat source model, requiring thus revaluating the validity of this model in designing energy piles.

CRediT authorship contribution statement

Mehdi M. Arzanfudi: Conceptualization, Methodology, Software, Validation, Writing - original draft, Visualization. **Rafid Al-Khoury:** Conceptualization, Methodology, Validation, Writing - original draft, Supervision, Project administration. **L.J. Sluys:** Writing - review & editing, Supervision, Project administration. **G.M.A. Schreppers:** Writing - review & editing.

Declaration of Competing Interest

The authors declare that they have no known competing financial interests or personal relationships that could have appeared to influence the work reported in this paper.

Acknowledgements

The authors acknowledge the financial support by NWO (Netherlands Organization for Scientific Researc) under grant number 14698. They highly appreciate the in-kind contributions and technical support of FUNDEX (piles company), Deltares (geotechnics consultancy company) and DIANA FEA (finite element company). They are grateful to the Green Village, Delft for accommodating the energy pile field experiment.

Appendix A:. Water equations of state

The water equations of state (EOS) is established by adopting subcooled liquid water EOS from IAPWS [21], and ice–supercooled water mixture EOS from other relevant literature, given hereafter.

Liquid water:

Specific enthalpy [34,21]:

$$h_{lw}(p_m, T_m) = \begin{cases} R_{\mathrm{H2O}} T_m T_m^{*2} \dfrac{\partial \gamma}{\partial p_m^*} & T_m \geqslant T_f \\ h_{lw}|_{T_f} + \int_{T_f}^{T_m} \dfrac{1}{18.01528 \times 10^{-3}} \left[0.044 \left(\dfrac{T_m}{222} - 1 \right)^{-2.5} + 74.3 \right] dT & T_m < T_f \end{cases} \tag{A.1}$$

in which R_{H2O} is the specific gas constant for water, $p_m^* = p_m/16.53 \times 10^6$, $T_m^* = 1386.0/T_m$ and

$$\gamma(p_m^*, T_m^*) = \sum_{i=1}^{34} n_i (7.1 - p_m^*)^{I_i} (T_m^* - 1.222)^{J_i} \tag{A.2}$$

where n_i, I_i and J_i are material constants.

Density [20,21]:

$$\rho_{lw}(p_m, T_m) = \begin{cases} \dfrac{p_m}{R_{\mathrm{H2O}} T_m p_m^* \dfrac{\partial \gamma}{\partial p_m^*}} & T_m \geqslant T_f \\ -0.0228(T_m - 273.15)^2 - 0.1176(T_m - 273.15) + 999.9 & T_m < T_f \end{cases} \tag{A.3}$$

Viscosity [19,10]:

$$\mu_{lw}(p_m, T_m) = \begin{cases} \dfrac{100\sqrt{\dfrac{T_m}{647.096}}}{\sum_{i=0}^{3}\dfrac{H_i}{\left(\dfrac{T_m}{647.096}\right)^i}} e^{\frac{\rho_{lw}}{322.0}\sum_{i=0}^{5}\left(\frac{647.096}{T_m}-1\right)^i \sum_{j=0}^{6} H_{ij}\left(\frac{\rho_{lw}}{322.0}-1\right)^j} e^{0.068Y} & T_m \geqslant T_f \\ 5.0\times10^{-6}(T_m-273.15)^2 - 3.0\times10^{-5}(T_m-273.15) + 0.0018 & T_m < T_f \end{cases} \tag{A.4}$$

where Y, H_i and H_{ij} are material constants.

Heat conductivity [6,28]:

$$\lambda_{lw}(T_m) = \begin{cases} 0.6065\left(-1.48445 + 4.12292\left(\dfrac{T_m}{298.15}\right) - 1.63866\left(\dfrac{T_m}{298.15}\right)^2\right) & T_m \geqslant T_f \\ 0.0017(T_m - 273.15) + 0.5583 & T_m < T_f \end{cases} \tag{A.5}$$

Ice:

Specific enthalpy [15]:

$$h_{ice}(T_m) = h_{ice}|_{T_f} + \int_{T_f}^{T_m}[185.0 + 6.89(T_m - 273.15)]dT$$
$$h_{ice}|_{T_f} = h_{lw}|_{T_f} - L_f \tag{A.6}$$

Density [15]:

$$\rho_{ice}(T_m) = 917.0(1. - 1.17\times10^{-4}(T_m - 273.15)) \tag{A.7}$$

Heat conductivity [15]:

$$\lambda_{ice}(T_m) = 1.16(1.91 - 8.66\times10^{-3}(T_m - 273.15) + 2.97\times10^{-5}(T_m - 273.15)^2) \tag{A.8}$$

Appendix B. Thermal interaction coefficients

Heat exchanger–Pile

The thermal interaction coefficient between the heat exchanger and the pile concrete is calculated as [4]

$$b_{cr} = \frac{1}{R_{conv} + R_{cond}} \tag{B.1}$$

where R_{conv} and R_{cond} are the thermal resistances, expressed as

$$R_{conv} = \frac{1}{r_o/r_i\bar{h}} \quad , \quad R_{cond} = \frac{r_o\ln(r_o/r_i)}{\lambda_p} \tag{B.2}$$

in which r_i and r_o are the inner and outer radius of the U-tube, λ_p is the thermal conductivity of the U-tube material, and $\bar{h}$ is the convective heat transfer coefficient, described as

$$\bar{h} = \frac{Nu\lambda_r}{2r_i} \tag{B.3}$$

where Nu is the Nusselt number, which might be defined as

$$Nu = \begin{cases} 0.664Re^{1/2}Pr^{1/3} & Re \leqslant 2000 \\ 0.023Re^{0.8}Pr^{0.4} & Re > 2000 \end{cases} \tag{B.4}$$

in which Pr and Re are the Prandtl and Reynolds numbers, described as

$$Pr = \frac{\mu_r c_r}{\lambda_r} \quad , \quad Re = \frac{\rho_r\ |v_r|(2r_i)}{\mu_r} \tag{B.5}$$

where ρ_r, c_r, μ_r, λ_r and v_r, denote the density, specific heat capacity, dynamic viscosity, thermal conductivity and velocity of the circulating fluid, respectively.

Pile–Soil

The thermal interaction coefficient the pile–soil interface is:

$$b_{sc} = \frac{1}{R_{sc}} \tag{B.6}$$

where R_{sc} are the thermal resistances, described as

$$R_{sc} = \frac{r_2\ln(r_2/r_1)}{\lambda_{\text{interface}}} \tag{B.7}$$

in which $r_2 - r_1$ represents the thickness of interface.

Soil–Air

The soil–air thermal interaction can be described as

$$b_{sa} = \frac{Nu\lambda_a}{L} \tag{B.8}$$

in which λ_a denotes the thermal conductivity of air, L is the length of the ground surface in the direction of air flow, and Nu is the Nusselt number, with relevant parameters for air.

Appendix C. Derivatives of constitutive terms

A sample derivation, namely for $\partial p_s/\partial h_m$, is given here. Other derivatives can be obtained in a similar way.
Eq. (24) indicates that S_{lw} and S_{ice} are functions of the mixture temperature, i.e.

$$\begin{aligned} S_{lw} &\equiv S_{lw}(T_m) \\ S_{ice} &= 1 - S_{lw} \equiv S_{ice}(T_m) \end{aligned} \tag{C.1}$$

By definition, the liquid and ice pressures are function of mixture pressure and cryogenic suction, as:

$$\begin{aligned} p_{lw} &= p_m - s_c \equiv p_{lw}(p_m, s_c) \\ p_{ice} &= p_{lw} + s_c \equiv p_{ice}(p_m, s_c) \end{aligned} \tag{C.2}$$

Similarly, Appendix A indicates that the specific enthalpy and mass density are functions of mixture pressure and temperature, as

$$\begin{aligned} h_{lw} &\equiv h_{lw}(p_m, T_m) \\ h_{ice} &\equiv h_{ice}(T_m) \\ \rho_{lw} &\equiv \rho_{lw}(p_m, T_m) \\ \rho_{ice} &\equiv \rho_{ice}(T_m) \end{aligned} \tag{C.3}$$

Eq. (C.3) indicates that the mixture temperature is a function of mixture pressure and specific enthalpy, as

$$T_m \equiv T_m(p_m, h_m) \tag{C.4}$$

Following these identities, the derivative on of Eq. (2) with respect to h_m can be described in terms of the constitutive relationships, as

$$\frac{\partial p_s}{\partial h_m} = \frac{\partial S_{lw}(p_m, h_m)}{\partial h_m} p_{lw}(p_m, s_c) + \frac{\partial S_{ice}(p_m, h_m)}{\partial h_m} p_{ice}(p_m, s_c) \tag{C.5}$$

Appendix D. FE matrices and vectors for 3D elements

Soil:

$$\boldsymbol{C}^s_{11} = -\int_{\Omega_s} \boldsymbol{B}^T \boldsymbol{D}^{ep} \boldsymbol{B} d\Omega_s \quad ; \quad \boldsymbol{C}^s_{12} = \int_{\Omega_s} \boldsymbol{B}^T \boldsymbol{m} \alpha \frac{\partial p_s}{\partial p_m} \boldsymbol{N} d\Omega_s + \int_{\Omega_s} \boldsymbol{N}_u^T \frac{\partial \rho_{eff}}{\partial p_m} \boldsymbol{g} \boldsymbol{N} d\Omega_s$$

$$\boldsymbol{C}^s_{13} = \int_{\Omega_s} \boldsymbol{B}^T \boldsymbol{m} \alpha \frac{\partial p_s}{\partial h_m} \boldsymbol{N} d\Omega_s + \int_{\Omega_s} \boldsymbol{N}_u^T \frac{\partial \rho_{eff}}{\partial h_m} \boldsymbol{g} \boldsymbol{N} d\Omega_s \quad ; \quad \boldsymbol{C}^s_{14} = \int_{\Omega_s} \boldsymbol{B}^T \boldsymbol{D}^{ep} \frac{1}{3} \boldsymbol{m} \beta_s \boldsymbol{N} d\Omega_s$$

$$\boldsymbol{C}^s_{15} = \int_{\Omega_s} \boldsymbol{B}^T \boldsymbol{m} \alpha \frac{\partial p_s}{\partial s_c} \boldsymbol{N} d\Omega_s \quad ; \quad \boldsymbol{C}^s_{21} = \int_{\Omega_s} \boldsymbol{N}^T \alpha \rho_m \boldsymbol{m}^T \boldsymbol{B} d\Omega_s$$

$$\boldsymbol{C}^s_{22} = \int_{\Omega_s} \boldsymbol{N}^T \left(\frac{\alpha - \varphi}{K_s} \rho_m \frac{\partial p_s}{\partial p_m} + \varphi \frac{\partial \rho_m}{\partial p_m} \right) \boldsymbol{N} d\Omega_s \quad ; \quad \boldsymbol{C}^s_{23} = \int_{\Omega_s} \boldsymbol{N}^T \left(\frac{\alpha - \varphi}{K_s} \rho_m \frac{\partial p_s}{\partial h_m} + \varphi \frac{\partial \rho_m}{\partial h_m} \right) \boldsymbol{N} d\Omega_s$$

$$\boldsymbol{C}^s_{24} = -\int_{\Omega_s} \boldsymbol{N}^T \rho_m \beta_s (\alpha - \varphi) \boldsymbol{N} d\Omega_s \quad ; \quad \boldsymbol{C}^s_{25} = \int_{\Omega_s} \boldsymbol{N}^T \frac{\alpha - \varphi}{K_s} \rho_m \frac{\partial p_s}{\partial s_c} \boldsymbol{N} d\Omega_s$$

$$\boldsymbol{C}^s_{31} = \int_{\Omega_s} \boldsymbol{N}^T [(1-\varphi) K_T - (\varphi - \alpha) \rho_m h_m - (\varphi - \alpha)(-p_m + p_s')] \boldsymbol{m}^T \boldsymbol{B} d\Omega_s$$

$$\boldsymbol{C}^s_{32} = \int_{\Omega_s} \boldsymbol{N}^T \left[(\rho_m h_m - p_m + p_s') \frac{\alpha - \varphi}{K_s} \frac{\partial p_s}{\partial p_m} - \varphi + \varphi h_m \frac{\partial \rho_m}{\partial p_m} \right] \boldsymbol{N} d\Omega_s$$

$$\boldsymbol{C}^s_{33} = \int_{\Omega_s} \boldsymbol{N}^T \left[\varphi \rho_m + \varphi h_m \frac{\partial \rho_m}{\partial h_m} + (\rho_m h_m - p_m + p_s') \frac{\alpha - \varphi}{K_s} \frac{\partial p_s}{\partial h_m} \right] \boldsymbol{N} d\Omega_s$$

$$\boldsymbol{C}^s_{34} = \int_{\Omega_s} \boldsymbol{N}^T [(1-\varphi) \rho_s c_s - \beta_s (\alpha - \varphi)(\rho_m h_m - p_m + p_s')] \boldsymbol{N} d\Omega_s$$

$$\boldsymbol{C}^s_{35} = \int_{\Omega_s} \boldsymbol{N}^T (\rho_m h_m - p_m + p_s') \frac{\alpha - \varphi}{K_s} \frac{\partial p_s}{\partial s_c} \boldsymbol{N} d\Omega_s \quad ; \quad \boldsymbol{K}^s_{22} = \int_{\Omega_s} \nabla \boldsymbol{N}^T \rho_{lw} \frac{\boldsymbol{k} k_{rlw}}{\mu_{lw}} \nabla \boldsymbol{N} d\Omega_s$$

$$\boldsymbol{K}^s_{25} = -\int_{\Omega_s} \nabla \boldsymbol{N}^T \rho_{lw} \frac{\boldsymbol{k} k_{rlw}}{\mu_{lw}} \nabla \boldsymbol{N} d\Omega_s \quad ; \quad \boldsymbol{K}^s_{32} = \int_{\Omega_s} \nabla \boldsymbol{N}^T \rho_{lw} h_{lw} \frac{\boldsymbol{k} k_{rlw}}{\mu_{lw}} \nabla \boldsymbol{N} d\Omega_s$$

$$\boldsymbol{K}^s_{34} = \int_{\Omega_s} \nabla \boldsymbol{N}^T \boldsymbol{\lambda}_{eff} \nabla \boldsymbol{N} d\Omega_s \quad ; \quad \boldsymbol{K}^s_{35} = -\int_{\Omega_s} \nabla \boldsymbol{N}^T \rho_{lw} h_{lw} \frac{\boldsymbol{k}\boldsymbol{k}_{rlw}}{\mu_{lw}} \nabla \boldsymbol{N} d\Omega_s \quad ; \quad \boldsymbol{K}^s_{44} = \int_{\Omega_s} \boldsymbol{N}^T \boldsymbol{N} d\Omega_s$$

$$\boldsymbol{K}^s_{55} = \int_{\Omega_s} \boldsymbol{N}^T \boldsymbol{N} d\Omega_s \quad ; \quad \boldsymbol{f}^s_1 = -\int_{\Gamma_q} \boldsymbol{N}^T_u \hat{\boldsymbol{t}} d\Gamma \quad ; \quad \boldsymbol{f}^s_2 = \int_{\Omega_s} \nabla \boldsymbol{N}^T \rho_{lw} \frac{\boldsymbol{k}\boldsymbol{k}_{rlw}}{\mu_{lw}} \rho_{lw} \boldsymbol{g} d\Omega_s - \int_{\Gamma_q} \boldsymbol{N}^T \hat{q}_{lw} d\Gamma$$

$$\boldsymbol{f}^s_3 = \int_{\Omega_s} \nabla \boldsymbol{N}^T \rho_{lw} h_{lw} \frac{\boldsymbol{k}\boldsymbol{k}_{rlw}}{\mu_{lw}} \rho_{lw} \boldsymbol{g} d\Omega_s - \int_{\Gamma_q} \boldsymbol{N}^T \hat{Q}_{\text{soil - air}} = d\Gamma \quad ; \quad \boldsymbol{f}^s_4 = \int_{\Omega_s} \boldsymbol{N}^T T_m d\Omega_s$$

$$\boldsymbol{f}^s_5 = -\int_{\Omega_s} \boldsymbol{N}^T \rho_{ice} L_f \ln \frac{T_m}{T_f} d\Omega_s \tag{D.1}$$

where $\boldsymbol{B} = \boldsymbol{L}\boldsymbol{N}_u$.

Concrete:

$$\boldsymbol{C}^c_{11} = -\int_{\Omega_c} \boldsymbol{B}^T \boldsymbol{D}_c \boldsymbol{B} d\Omega_c \quad ; \quad \boldsymbol{C}^c_{16} = \int_{\Omega_c} \boldsymbol{B}^T \boldsymbol{D}_c \boldsymbol{m} \frac{1}{3} \beta_c \boldsymbol{N} d\Omega_c \quad ; \quad \boldsymbol{C}^c_{66} = \int_{\Omega_c} \boldsymbol{N}^T \rho_c c_c \boldsymbol{N} d\Omega_c$$

$$\boldsymbol{K}^c_{66} = \int_{\Omega_c} \nabla \boldsymbol{N}^T \boldsymbol{\lambda}_c \nabla \boldsymbol{N} d\Omega_c \quad ; \quad \boldsymbol{f}^c_1 = -\int_{\Omega_c} \boldsymbol{N}^T_u \rho_c \boldsymbol{g} d\Omega - \int_{\Gamma_q} \boldsymbol{N}^T_u \hat{\boldsymbol{t}} \Gamma_q \quad ; \quad \boldsymbol{f}^c_6 = -\int_{\Gamma_q} \boldsymbol{N}^T \hat{Q}_{\text{cond}} \Gamma_q$$

$$\boldsymbol{f}^{cs} = -\boldsymbol{f}^{sc} = \int_{\Gamma^{sc}_q} \boldsymbol{N}^T Q^{sc} d\Gamma^{sc}_q \tag{D.2}$$

Interface:

$$\boldsymbol{C}^i_{11} = -\int_{\Omega_i} \boldsymbol{B}^T \boldsymbol{C}^{ep} \boldsymbol{B} d\Omega_i \quad ; \quad \boldsymbol{C}^i_{12} = \int_{\Omega_i} \boldsymbol{B}^T \boldsymbol{m} \alpha \frac{\partial p_s}{\partial p_m} \boldsymbol{N} d\Omega_i + \int_{\Omega_i} \boldsymbol{N}^T_u \frac{\partial \rho^i_{eff}}{\partial p_m} \boldsymbol{N} \boldsymbol{g} d\Omega_i$$

$$\boldsymbol{C}^i_{13} = \int_{\Omega_i} \boldsymbol{B}^T \boldsymbol{m} \alpha \frac{\partial p_s}{\partial h_m} \boldsymbol{N} d\Omega_i + \int_{\Omega_i} \boldsymbol{N}^T_u \frac{\partial \rho^i_{eff}}{\partial h_m} \boldsymbol{N} \boldsymbol{g} d\Omega_i \quad ; \quad \boldsymbol{C}^i_{14} = \int_{\Omega_i} \boldsymbol{B}^T \boldsymbol{C}^{ep} \boldsymbol{m} \frac{1}{3} \beta_i \boldsymbol{N} d\Omega_i$$

$$\boldsymbol{C}^i_{15} = \int_{\Omega_i} \boldsymbol{B}^T \boldsymbol{m} \alpha \frac{\partial p_s}{\partial s_c} \boldsymbol{N} d\Omega_i \quad ; \quad \boldsymbol{C}^i_{16} = \int_{\Omega_i} \boldsymbol{B}^T \boldsymbol{C}^{ep} \boldsymbol{m} \frac{1}{3} \beta_i \boldsymbol{N} d\Omega_i \tag{D.3}$$

and $\boldsymbol{K}^{\mathrm{i}}_{2\mathrm{j}} \equiv \boldsymbol{K}^{\mathrm{s}}_{2\mathrm{j}}$ and $\boldsymbol{C}^{\mathrm{i}}_{2\mathrm{j}} \equiv \boldsymbol{C}^{\mathrm{s}}_{2\mathrm{j}}$.

References

Al-Khoury, R., 2011. Computational modeling of shallow geothermal systems. CRC Press.

Amatya, B.L., Soga, K., Bourne-Webb, P.J., Laloui, L., 2012. Thermo-mechanical behaviour of energy piles. Geotechn-Lond 62, 503–519.

Anongphouth, A., Maghoul, P., Alfaro, M., 2018. Numerical modeling of concrete energy piles using a coupled thermo-hydro-mechanical model. GeoEdmonton 2018 Conference, Edmonton, Alberta, Canada, September 23-26.

Arzanfudi, M.M., Al-Khoury, R., 2015. A compressible two-fluid multiphase model for CO2 leakage through a wellbore. Int J Numer Meth Fluids 77 (8), 477–507.

Arzanfudi, M.M., Al-Khoury, R., 2018. Freezing-thawing of porous media: an extended finite element approach for soil freezing and thawing. Adv Water Resour 119, 210–226.

Benchikh, O., Fournier, D., Boccara, A., Teixeira, J., 1985. Photothermal measurement of the thermal conductivity of supercooled water. J Phys 46 (5), 727–731.

Bourne-Webb, P., Amatya, B., Soga, K., Amis, T., Davidson, C., Payne, P., 2009. Energy pile test at Lambeth College, London: geotechnical and thermodynamic aspects of pile response to heat cycles. Géotechnique 59 (3), 237–248.

Brooks, R.H., Corey, A.T., 1964. Hydraulic Properties of Porous Media. Hydrology Papers. Colorado State University (March).

Chen, W.-F., Baladi, G.Y., 1985. Soil plasticity: theory and implementation, vol. 38 Elsevier.

Cooper, J., Dooley, R., 2008. Release of the IAPWS formulation 2008 for the viscosity of ordinary water substance. The International Association for the Properties of Water and Steam.

Desai, C., Zaman, M., Lightner, J., Siriwardane, H., 1984. Thin-layer element for interfaces and joints. Int J Numer Anal Meth Geomech 8 (1), 19–43.

Di Donna, A., Laloui, L., 2015. Numerical analysis of the geotechnical behaviour of energy piles. Int J Numer Anal Meth Geomech 39 (8), 861–888.

Di Donna, A., Rotta Loria, A.F., Laloui, L., 2016. Numerical study of the response of a group of energy piles under different combinations of thermo-mechanical loads. Comput Geotech 72, 126–142.

François, B., Laloui, L., 2008. ACMEG-TS: A constitutive model for unsaturated soils under non-isothermal conditions. Int J Numer Anal Meth Geomech 32 (16), 1955–1988.

Fukusako, S., 1990. Thermophysical properties of ice, snow, and sea ice. Int J Thermophys 11 (2), 353–372.

Gawecka KA, Taborda DM, Potts DM, Cui W, Zdravkovic L, Haji Kasri M. Numerical modelling of thermo-active piles in London Clay; 2016.

Gawin, D., Pesavento, F., Koniorczyk, M., Schrefler, B.A., 2019. Non-equilibrium modeling hysteresis of water freezing: Ice thawing in partially saturated porous building materials. J Build Phys 43 (2), 61–98.

Geiser, F., Laloui, L., Vulliet, L.: Modelling the behaviour of unsaturated silt. Experimental evidence and theoretical approaches in unsaturated soils. Balkema, Rotterdam, 155-175 (2000).

Hallett, J., 1963. The temperature dependence of the viscosity of supercooled water. Proc Phys Soc 82 (6), 1046.

Hare, D., Sorensen, C., 1987. The density of supercooled water. II. Bulk samples cooled to the homogeneous nucleation limit. J Chem Phys 87 (8), 4840–4845.

IAPWS: Revised release on the IAPWS industrial formulation 1997 for the thermodynamic properties of water and steam. In: The International Association for the Properties of Water and Steam; 2007.

Koniorczyk, M., Gawin, D., Schrefler, B.A., 2015. Modeling evolution of frost damage in fully saturated porous materials exposed to variable hygro-thermal conditions. Comput Methods Appl Mech Eng 297, 38–61.

Kurylyk, B.L., Watanabe, K., 2013. The mathematical representation of freezing and thawing processes in variably-saturated, non-deformable soils. Adv Water Resour 60, 160–177.

Laloui, L., Cekerevac, C., 2003. Thermo-plasticity of clays: an isotropic yield mechanism. Comput Geotech 30 (8), 649–660.

Laloui, L., François, B., 2009. ACMEG-T: soil thermoplasticity model. J Eng Mech 135 (9), 932–944.

Lewis, R.W., Schrefler, B.A., 1998. The finite element method in the static and dynamic deformation and consolidation of porous media, 2nd ed. John Wiley & Sons, Chichester.

Mimouni, T., Laloui, L., 2015. Behaviour of a group of energy piles. Can Geotech J 52 (12), 1913–1929.

Ramires M, de Castro CN, Nagasaka Y, Nagashima A. Standard Reference Data for the Thermal Conductivity of Water; 1994.

Rotta Loria, A.F., Donna, A.D., Laloui, L., 2015. Numerical study on the suitability of centrifuge testing for capturing the thermal-induced mechanical behavior of energy piles. J Geotech Geoenviron Eng 141 (10), 04015042.

Rotta Loria, A.F., Gunawan, A., Shi, C., Laloui, L., Ng, C.W., 2015. Numerical modelling of energy piles in saturated sand subjected to thermo-mechanical loads. Geomech Energy Environ 1, 1–15.

Rotta Loria, A.F., Laloui, L., 2017. Thermally induced group effects among energy piles. Géotechnique 67 (5), 374–393.

Suryatriyastuti, M., Mroueh, H., Burlon, S., 2012. Understanding the temperature-induced mechanical behaviour of energy pile foundations. Renew Sustain Energy Rev 16 (5), 3344–3354.

Sutman, M., Olgun, C.G., Laloui, L., 2018. Cyclic load-transfer approach for the analysis of energy piles. J Geotech Geoenviron Eng 145 (1), 04018101.

Tombari, E., Ferrari, C., Salvetti, G., 1999. Heat capacity anomaly in a large sample of supercooled water. Chem Phys Lett 300 (5–6), 749–751.

Yavari, N., Tang, A.M., Pereira, J.-M., Hassen, G., 2014. A simple method for numerical modelling of energy pile's mechanical behaviour. Géotech Lett 4 (April-June), 119–124.

Goodman, R.E., Taylor, R.L., Brekke, T.L., 1968. A model for the mechanics of jointed rock. J Soil Mech Found Div 94, 637–659.

Zienkiewicz, O.C., Best, B., Dullage, C., Stagg, K.G., 1970. Analysis of nonlinear problems with particular reference to jointed rock systems. Proc 2nd Intl Conf Soc Rock Mech, Belgrade 3, 501–509.